The Prolyl-tRNA Synthetase Inhibitor Halofuginone Inhibits SARS-CoV-2 Infection

Daniel R. Sandoval[1,2,#], Thomas Mandel Clausen[2,3,#], Chelsea Nora[1,#], Jason A. Magida[4], Adam P. Cribbs[5], Andrea Denardo[1,6], Alex E. Clark[1,2], Aaron F. Garretson[1], Joanna K.C. Coker[1,7], Anoop Narayanan[8], Sydney A. Majowicz[8], Martin Philpott[5], Catrine Johansson[5], James E. Dunford[5], Charlotte B. Spliid[2], Gregory J. Golden[2,9], N. Connor Payne[10,11], Mark A. Tye[10,12], Cameron J. Nowell[13], Eric R. Griffis[14], Ann Piermatteo[1], Kaare V. Grunddal[1], Thibault Alle[15], Blake M. Hauser[16], Jared Feldman[17], Timothy M. Caradonna[18], Yuan Pu[19], Xin Yin[17], Rachael N. McVicar[7,18,19], Elizabeth M. Kwong[7,18,19], Sotirios Tsimikas[1], Aaron G. Smidt[16,20], Carlo Ballatore[15], Karsten Zengler[7,21,22], Sumit K. Chanda[17], Ryan J. Weiss[2,23], Michael Downes[4], Ron M. Evans[4,24], Ben A. Croker[7], Sandra L. Leibel[7,18,19], Joyce Jose[8], Ralph Mazitschek[10,25,26], Udo Oppermann[5,27], Jeffrey D. Esko[2,28], Aaron F. Carlin[1,*], Philip L.S.M. Gordts[1,28,*]

[1]Department of Medicine, University of California, San Diego, La Jolla, CA 92093, USA. [2]Department of Cellular and Molecular Medicine, University of California, San Diego, La Jolla, CA 92093, USA. [3]Copenhagen Center for Glycomics, Department of Molecular and Cellular Medicine, Faculty of Health and Medical Sciences, University of Copenhagen, 2200 Copenhagen, Denmark. [4]Gene Expression Laboratory, Salk Institute for Biological Studies, La Jolla, CA, USA. [5]Botnar Research Centre, NIHR Biomedical Research Centre, University of Oxford, OX3 7LD, UK. [6]Department of Molecular and Translational Medicine, University of Brescia, Brescia, Italy. [7]Department of Pediatrics, University of California, San Diego, La Jolla, CA 92037, USA. [8]Department of Biochemistry and Molecular Biology, The Huck Institutes of the Life Sciences, The Pennsylvania State University, University Park, PA, 16802, USA. [9]Biomedical Sciences Graduate Program, University of California San Diego, La Jolla, CA, USA. [10]Center for Systems Biology, Massachusetts General Hospital, Boston, MA, 02114, USA. [11]Department of Chemistry &

Chemical Biology, Harvard University, Cambridge, MA, 02114, USA. [12]Harvard Graduate School of Arts and Sciences, Cambridge, MA, 02138, USA. [13]Monash Institute of Pharmaceutical Sciences, Victoria 3052, Australia. [14]Nikon Imaging Center, University of California, San Diego, La Jolla, CA 92037, USA. [15]Skaggs School of Pharmacy and Pharmaceutical Sciences, University of California, San Diego, La Jolla, California, USA. [16]Ragon Institute of MGH, MIT and Harvard, Cambridge, MA 02139, USA.[17]Immunity and Pathogenesis Program, Infectious and Inflammatory Disease Center, Sanford Burnham Prebys Medical Discovery Institute, La Jolla, CA 92037, USA. [18]Sanford Burnham Prebys Medical Discovery Institute, La Jolla, CA 92037, USA. [19]Sanford Consortium for Regenerative Medicine, La Jolla, CA 92037, USA. [20]Department of Microbiology, Harvard Medical School, Cambridge, MA, 02115 USA. [21]Department of Bioengineering, University of California, San Diego, 9500 Gilman Drive, La Jolla, CA 92093-0412, USA. [22]Center for Microbiome Innovation, University of California, San Diego, 9500 Gilman Drive, La Jolla, CA, 92093-0436, USA. [23]Complex Carbohydrate Research Center, Department of Biochemistry and Molecular Biology, University of Georgia, Athens GA, USA. [24]Howard Hughes Medical Institute, Salk Institute for Biological Studies, La Jolla, CA, USA. [25]Harvard T.H. Chan School of Public Health, Cambridge, MA, 02115, USA. [26]Broad Institute of MIT and Harvard, Cambridge, MA, 02142, USA. [27]Centre for Medicines Discovery, University of Oxford, UK. [28]Glycobiology Research and Training Center, University of California, San Diego, La Jolla, CA 92093, USA.

[#]Contributed equally to the work.

*To whom correspondence should be addressed: Philip L.S.M. Gordts, Department of Medicine, University of California, La Jolla, CA 92093, USA; +1(858)246-0994, pgordts@health.ucsd.edu, Aaron F. Carlin, Department of Medicine, University of California, La Jolla, CA 92093, USA; +1(858)246-3261, acarlin@health.ucsd.edu

SUMMARY

We identify the prolyl-tRNA synthetase (PRS) inhibitor halofuginone, a compound in clinical trials for anti-fibrotic and anti-inflammatory applications, as a potent inhibitor of SARS-CoV-2 infection and replication. The interaction of SARS-CoV-2 spike protein with cell surface heparan sulfate (HS) promotes viral entry. We find that halofuginone reduces HS biosynthesis, thereby reducing spike protein binding, SARS-CoV-2 pseudotyped virus, and authentic SARS-CoV-2 infection. Halofuginone also potently suppresses SARS-CoV-2 replication post-entry. Utilizing analogues of halofuginone and small molecule inhibitors of the PRS, we establish that inhibition of HS presentation and viral replication is dependent on proline tRNA synthesis opposed to PRS activation of the integrated stress response (ISR). Moreover, we provide evidence that these effects are mediated by the depletion of proline tRNAs. In line with this, we find that SARS-CoV-2 polyproteins, as well as several HS proteoglycans, are particularly proline-rich, which may make them vulnerable to halofuginone translational suppression. Halofuginone is orally bioavailable, has been evaluated in a phase I clinical trial in humans and distributes to SARS-CoV-2 target organs, including the lung, making it a promising clinical trial candidate for the treatment of COVID-19.

INTRODUCTION

Severe acute respiratory syndrome-related coronavirus 2 (SARS-CoV-2), the causative agent of coronavirus disease 2019 (COVID-19), has swept across the globe causing over 100 million infections and over 2 million confirmed deaths (2020b). The US Food and Drug Administration (FDA) has granted an Emergency Use Authorization (EUA) for Remdesivir (RDV, GS-5734) for the treatment of hospitalized patients with severe COVID-19 (2020a). However, data from multiple trials suggests that Remdesivir provides modest clinical benefit compared with standard of care (Beigel et al., 2020; Spinner et al., 2020; Wang et al., 2020). Hence, the use of Remdesivir in patients with COVID-19 was discouraged by the World Health Organization in November 2020. Convalescent plasma from individuals who have recovered from COVID-19 has also been granted EUA for hospitalized patients with COVID-19 but efficacy data from randomized trials are needed. And despite massive roll-out of vaccines against SARS-CoV-2, the rapid emergence of novel strains amongst other practical issues raises serious concerns on the longevity and efficacy of this approach to confer herd immunity (Hie et al., 2021). Hence, there is an urgent unmet clinical need for an arsenal of potent antiviral therapeutics that can reduce COVID-19 associated morbidity and mortality (McCreary and Angus, 2020; Thorp, 2020).

Analogous to SARS-CoV, viral entry of SARS-CoV-2 is dependent on the viral spike protein binding to the host receptor ACE2 after spike protein priming by the host serine protease TMPRSS2 (Hoffmann et al., 2020). However, unlike SARS-CoV, infection of lung upper airway epithelial cells by SARS-CoV-2 depends on heparan sulfate (HS)-mediated enhancement of SARS-CoV-2 spike protein binding to ACE2 (Clausen et al., 2020; Hoffmann et al., 2020; Mycroft-West et al., 2020). Blocking the interaction of the spike protein with cell surface HS inhibits SARS-CoV-2 binding and attenuates SARS-CoV-2 infection (Clausen et al., 2020). HS is a linear polysaccharide attached to the protein core of HS proteoglycans (HSPGs) (Pessentheiner et al., 2020). HS is universally expressed in all tissues and due to its length (40-300 sugar residues) it

makes up a large part of the cell-associated glycocalyx which is targeted by a myriad of viruses (Sarrazin et al., 2011). Currently, HS-derivatives, such as heparinoids, are being tested for their capacity as antivirals to inhibit SARS-CoV-2 infection, by inhibiting spike protein mediated binding to the host cells. In addition to direct viral neutralization, modulating HS presentation on the host cells may provide an alternative approach to control viral infection.

In this report, we screened a small molecule library composed of epigenetic and translation inhibitors for their capacity to block HS cell surface presentation and thereby SARS-CoV-2 binding. We identified halofuginone, a synthetic analog of the natural product febrifugine that is derived from *Dichroa febrifuga* (one of the 50 fundamental herbs of traditional Chinese medicine), as a potent inhibitor of HS biosynthesis and SARS-CoV-2 infection (Keller et al., 2012; Pines and Spector, 2015). We demonstrate that halofuginone reduces HS biosynthesis, thereby decreasing SARS-CoV-2 spike protein binding to cells, infection with SARS-CoV-2 spike protein pseudotyped VSV virus, and infection by authentic SARS-CoV-2. Additionally, halofuginone inhibited authentic SARS-CoV-2 intra-host replication. Inhibition of prolyl-tRNA synthetase (PRS) activity was responsible for both the HS-dependent and the HS-independent antiviral properties of halofuginone. These findings identify halofuginone as a translational regulator of cell surface HS biosynthesis and a potentially potent therapeutic for the treatment and prevention of COVID-19.

RESULTS

Halofuginone Reduces SARS-CoV-2 Spike Protein and SARS-CoV-2 Spike Protein Pseudotyped Virus Binding

To identify agents that attenuate SARS-CoV-2 spike protein binding, we screened a library of small-molecule antagonists of host epigenetic regulators and protein translation elements along with their chemically matched inactive analogs (Cottone et al., 2020; Cribbs et al., 2018; Cribbs

et al., 2020). The compound library has been successfully used to investigate targets mediating anti-inflammatory or anti-proliferative effects in a variety of biological contexts (Cottone et al., 2020; Cribbs et al., 2018; Cribbs et al., 2020) and importantly, contains several FDA-approved drugs, which may facilitate rapid deployment for treatment of COVID-19 patients. Hep3B human hepatoma cells were treated with the compound library at the indicated concentrations (Fig. 1a & **Supplemental Table 1**) for 18 h, and binding of SARS-CoV-2 spike protein was assessed using recombinant receptor binding domain (RBD; from isolate Wuhan 20) in flow cytometry (Fig. 1a). As a positive control, cells were treated with a mixture of heparin lyases, which digest cell surface HS chains (Clausen et al., 2020). Class 1 histone deacetylase inhibitors, such as Romidepsin (1 μM) or Belinostat (5 μM), decreased SARS-CoV-2 RBD binding by ~50% compared to excipient control (DMSO; Fig 1a). Halofuginone (1 μM) reduced binding by 84%, a level of reduction similar to the impact of heparin lyase treatment (Fig 1a). This reduction was dose dependent (Fig 1b). Halofuginone targets the prolyl-tRNA synthetase (PRS) active site of the human glutamyl-prolyl tRNA synthetase (EPRS) and has been used in clinical and preclinical studies to treat fibrotic disease and to attenuate hyperinflammation (Pines and Spector, 2015; Zhou et al., 2013). To assay the ability of halofuginone to inhibit spike protein binding to a variety of cell lines permissive to SARS-CoV-2 infection, we treated Caco-2 human epithelial colorectal adenocarcinoma cells with halofuginone. Halofuginone reduced RBD protein binding to Hep3B and Caco-2 (Fig. 1b-c). The maximal degree of inhibition was equal in both cell lines. To test the effect of halofuginone treatment on the binding of spike protein in a more native presentation, we examined the ability of halofuginone to inhibit infection of SARS-CoV-2 spike protein pseudotyped VSV virus in Hep3B cells. Halofuginone inhibited SARS-CoV-2 spike protein pseudotyped VSV virus infection by up to ~30-fold in a dose-dependent manner (Fig. 1e).

Halofuginone Prevents Authentic SARS-CoV-2 Virus Infection of Human Bronchial Epithelial Cells.

We next tested if halofuginone inhibits the infection of authentic SARS-CoV-2 in Hep3B. Cells were treated with halofuginone at different doses for 24 h prior to and during infection (MOI of 0.1) (Fig. 2a) (Blight et al., 2002). The culture medium was collected, and the presence of infectious virus was measured by plaque assay. No infectious SARS-CoV-2 could be detected in the supernatants of Hep3B cells treated with halofuginone at doses greater than 50 nM (Fig. 2a), without affecting cell viability (Fig. 2b). Similarly, in Huh 7.5 cells, another human hepatoma cell line permissive to authentic SAS-CoV-2 infection, halofuginone inhibited productive SARS-CoV-2 infection with an IC_{50} of 109.4 nM (Fig. 2c) without affecting cell viability (Fig. 2d).

To explore the effect of halofuginone on SARS-CoV-2 infection in a more clinically relevant model, we infected primary human bronchial epithelial cells grown at an air-liquid interface with authentic SARS-CoV-2 virus with and without halofuginone treatment. Infection was monitored by flow cytometry using antibodies against the viral nucleocapsid protein (Fig. 2e). Halofuginone significantly reduced the number of SARS-CoV-2 infected cells at both 10 nM and 100 nM (Fig. 2f,g) without affecting cell viability (Fig. 2h). The data confirm that halofuginone is a potent inhibitor of authentic SARS-CoV-2 virus infection in primary human bronchial epithelial cells.

Halofuginone Inhibits Heparan Sulfate Biosynthesis

Given that binding of SARS-CoV-2 spike protein to cells is HS-dependent (Clausen et al., 2020), we evaluate the ability of halofuginone to inhibit cell surface HS presentation. Hep3B cells were treated for 18 h with halofuginone and the effects on cellular HS were evaluated using cell surface binding of the monoclonal antibody (mAb) (10E4) that recognizes a common epitope in HS (Fig. 3a). Halofuginone dose dependently reduced HS presentation as shown by staining with 10E4 (Fig 3b). The HS polysaccharides consist of alternating residues of *N*-acetylated or *N*-sulfated glucosamine (GlcNAc or GlcNS) and either glucuronic acid (GlcA) or iduronic acid (IdoA). Structural heterogeneity occurs due to the action of multiple sulfotransferases that add sulfate moieties to three different hydroxyl carbon positions (C2 on IdoA or C3 and C6 on GlcNAc) or on

the amine group (GlcNS) (**Supplemental Fig. 1a)**. The sulfated regions of the chains make up binding sites for various protein ligands, collectively known as the HS-interactome (Xu and Esko, 2014). To further characterize the effects halofuginone has on HS presentation, we treated Hep3B and quantified the amount of HS and its sulfation composition by mass spectrometry. When Hep3B cells were treated with 0.5 μM halofuginone, the total amount of HS was reduced by ~4-fold (Fig 3c) in line with the decrease in cell surface 10E4 binding (Fig 3b). Interesting, halofuginone treatment did not change the sulfation pattern (Fig. 3d), suggesting that the decrease in 10E4 staining (Fig 3a) is reflected in a decrease in total HS levels as opposed to a change in overall sulfation.

To investigate whether this reduction in cellular HS presentation is due to an effect on mRNA transcript levels of essential HS biosynthesis enzymes and core HSPGs, we preformed RNA-Seq analysis on Hep3B cells treated with vehicle or halofuginone at 200 or 500 nM for 6 h and 18 h. Halofuginone profoundly impacted the transcriptome in general (~2700 differentially expressed genes), which increased with longer incubation time (**Supplemental Fig. 1b-c**). Principal component analysis of RNA sequencing (RNA-seq) data clearly segregated the response with respect to the treatment duration (**Supplemental Fig. 1b**). Analysis of halofuginone upregulated genes did not identify common pathways associated with antiviral or inflammatory responses (**Supplemental Fig. 1d-e**) (Zhou et al., 2019). Additionally, no significant difference in expression of host factors exploited by SARS-CoV-2, such as *TMPRSS2* and *ACE2*, were observed (Fig. 3e). Gene annotation analysis of downregulated genes at 6 h showed that 200 nM halofuginone altered the expression of genes involved in glycoprotein biosynthesis and proteoglycan metabolic processes (**Supplemental Fig. 1e**) (Zhou et al., 2019). Only a select group of core HSPGs were downregulated at the mRNA level (Fig. 3e). In particular, HSPG core two proteins *GPC2* and *SDC1* were significantly downregulated in conjunction with two HS biosynthetic elongation enzymes *B3GAT3* and *EXTL3* (Fig. 3e). Taken together, the data

demonstrates that halofuginone suppresses the transcription of proteins involved in HS polymerization and HSPG presentation.

Given the observed effect on the transcription of known HS core proteins, we next investigated whether part of halofuginone's effects on HS presentation was due to a decrease in the availability of HS protein acceptor sites. To test this, we treated Hep3B cells with halofuginone, and then detected HSPG acceptor sites using a mAb (3G10) that recognizes a neo-epitope remaining on the proteoglycans after heparin lyase treatment via western blot (Fig. 3a) (David et al., 1992). The analysis revealed that halofuginone reduced HSPG core proteins, available to carry HS, in a dose-dependent manner (Fig. 3f & **Supplemental Fig. 1f**). These data suggest that halofuginone predominantly inhibits HS-mediated binding of the SARS-CoV-2 spike protein to cells by inhibiting the expression of core HSPGs.

Halofuginone Inhibition of Heparan Sulfate presentation and Spike Protein Binding Depends on Prolyl-tRNA Synthetase Targeting

Halofuginone belongs to a family of aminoacyl-tRNA-synthetases (AARS) inhibitors. AARS catalyze the ATP-dependent synthesis of amino-acylated tRNAs via a two-step reaction involving an aminoacyl-adenylate intermediate with subsequent transfer of amino group to the cognate tRNAs (Francklyn and Mullen, 2019). Halofuginone and chemically unrelated compounds like prolyl-sulfamoyl adenosine (ProSA), specifically and potently inhibit the human EPRS by blocking distinct portions of its ligand binding pocket in the PRS unit (Fig. 4a-b) (Adachi et al., 2017; Keller et al., 2012). Specifically, halofuginone competes with proline for the PRS active site (Fig. 4a) (Keller et al., 2012).

To better understand the relationship between PRS inhibition and HS expression and Spike RBD binding we tested related PRS inhibitor analogs to deconstruct the PRS pathway in relation to HS biosynthesis and SARS-CoV-2 spike RBD binding. Treatment with the non-cleavable and highly selective prolyl-AMP substrate analog ProSA at 5 μM prevented HS

presentation as illustrated by mAb 10E4 staining, and spike RBD binding to similar levels as treatment with halofuginone (500 nM) (Fig. 4c) (Kamtekar et al., 2003). Additionally, halofuginol (HFol), a halofuginone derivative that inhibits PRS, significantly decreased 10E4 and spike RBD binding. In contrast, MAZ1310 a halofuginone derivative in which the secondary amine is blocked as carbamate (Fig. 4a) and therefore cannot bind to PRS, had no effect (Fig. 4c-d) (Adachi et al., 2017; Keller et al., 2012). The commercial halofuginone used in our experiments is a racemate of two, 2*S*,3*R*-(-) and 2*R*,3*S*-(+) enantiomers (Jain et al., 2015). Only the 2*R*,3*S*-(+) enantiomers inhibits the PRS. As a control for specific PRS inhibition, we tested the two enantiomers separately. Only the 2*R*,3*S*-(+) enantiomer inhibited HS presentation and SARS-CoV-2 spike protein binding confirming that inhibition is due to the PRS inhibition and not off-target effects caused by the molecule itself (Fig. 4e-f). Collectively, these data demonstrate that PRS inhibition is sufficient to reduce HS presentation and spike RBD binding.

Halofuginone inhibits protein synthesis by competing with proline at the active site of the PRS (Herman et al., 2015). Therefore, we attempted to rescue HS presentation by adding excess proline. Proline (4mM) added to the media of Hep3B cells prevented the dose depended reduction of HSPG core proteins as measured by 3G10 Western blotting (Fig. 4g). In conjunction, excess proline prevented halofuginone from inhibiting RBD protein binding to the cells (Fig. 4h). Thus, halofuginone inhibits HS presentation and spike RBD binding by competitively inhibiting the PRS.

Our data suggest that PRS inhibitors, such as halofuginone, inhibit HS and HSPG expression both at the translational and transcriptional level (Fig. 3e,g). However, recently it has been reported that translational inhibition by PRS targeting may be mediated by a protein's sensitivity to limitation of proline incorporation in the growing polypeptide chain (Wu et al., 2020). Thereby PRS inhibitors can selectively modulate the translational efficiency of proline codon rich proteins, such as profibrotic collagens (Wu et al., 2020). To predict which HSPGs are more prone to PRS inhibition, we developed an proline distribution score to quantify and visualize proline density and distribution across proteins of interest. Using this index the proline codon rich

collagens generated a high proline distribution scores as compared to other proteins, such as TMPRSS2, ACE2 and lysosomal or cholesterol biosynthetic proteins (fig. 4i). Interestingly, HSPGs, such as agrin, perlecan, collagen 18, and syndecans 1 and 3, are relatively proline-enriched comparable to the collagen family (Fig. 4i, **Supplemental Fig. 2 and Supplemental Table 2**). These observations suggest that inhibition of prolyl-tRNA charging can particularly impair protein production of these key cell membrane and extracellular matrix HSPGs (Fig. 4i and 3g).

Halofuginone Inhibition of Spike Protein Binding to Heparan Sulfate is Independent of the Canonical Integrated Stress Response.

In addition to translational suppression of proline-rich proteins, PRS inhibition also triggers inhibition of global protein biosynthesis via General Control Nonderepressible 2 (GCN2)-mediated activation of the Integrated Stress Response (ISR) (Fig. 5a) (Keller et al., 2012). GCN2 (gene symbol *EIF2AK4*) senses uncharged tRNAs and phosphorylates the eukaryotic transcription initiation factor 2α (eIF2α), leading to a general reduction in 5'cap-mediated RNA translation and selective translation of the eukaryotic transcription factor ATF4 and its target genes (Fig. 5a) (Costa-Mattioli and Walter, 2020). These genes contain structural features in their 5'UTR allowing for selective translation in the presence of Ser51 phosphorylated eIF2α. The complexity and transient nature of the transcriptional and translational changes mediated by different eIF2α kinases of the ISR allows a cell to adapt and resolve various stress situations including amino acid starvation or unfolded protein stress (Costa-Mattioli and Walter, 2020).

When Hep3B cells were treated with halofuginone, RNA-seq analysis revealed a halofuginone mediated induction of a ISR target genes, including PPP1R15A, FGF21, DDIT3, and ATF4, whereas it did not activate genes associated with the unfolded protein-induced ER stress response (ER-SR) (Fig 4b) (Fusakio et al., 2016). To date, alterations in HS biosynthesis

have not been identified as a hallmark of the ISR. Hence, we determined if halofuginone suppresses HS biosynthesis by activating the ISR via co-incubation of halofuginone in the presence of a general inhibitor of the ISR, ISRIB (Integrated Stress Response inhibitor), or selective eIF2α kinase inhibitors GCN2-IN-1 (GCN2i) targeting GCN2, or GSK2606414 (PERKi) targeting protein kinase R-like endoplasmic reticulum kinase (PERK) (Fig. 5a) (Costa-Mattioli and Walter, 2020; Nakamura et al., 2018). Neither PERKi nor ISRIB had direct effects on 10E4 or RBD binding (Fig. 5c-d). In contrast, GCN2i reduced 10E4 and spike RBD binding almost to the same extent as halofuginone activity (Fig. 5c-d), suggesting a role for GCN2 in the regulation of HS biosynthesis independent of the ISR. However, none of the ISR inhibitors reversed or attenuated the halofuginone-induced reduction in 10E4 or spike protein binding, implying that this suppression is independent of ISR activation (Fig. 5c,d).

Halofuginone Inhibits Viral Binding and Replication by Authentic SARS-CoV-2 Virus

Initial translation of viral RNA after entry in the host cell is a crucial step for the propagation of SARS-CoV-2 and the manifestation of COVID-19. Given the potential role of proline incorporation during this translation process we examined the proline codon content and density of proteins encoded in the SARS-CoV-2 genome using our proline distribution score. The large SARS-CoV-2 coronavirus polyproteins, R1A (>400 kDa) and R1AB (>700 kDa), have high proline distribution scores comparable to collagens (Fig. 6a & **Supplemental Fig. 3a**). Interestingly, these proline distribution scores are conserved across the polyproteins of multiple members of the coronavirus family as well as other positive-sense single-stranded RNA viruses (**Supplemental Fig. 3b**), including Zika virus, Dengue virus, and Chikungunya that have been shown to be inhibited by halofuginone (**Supplemental Fig. 3c,d**) (Hwang et al., 2019).

R1A and R1AB are very large polyproteins that undergo proteolytic processing into 11 or 16 non-structural proteins, respectively, and are required for production of the SARS-CoV-2 viral RNA-dependent RNA polymerase (Nsp12) (Gordon et al., 2020). Because of this, we tested if

halofuginone was inhibitory after viral entry. We infected Huh7.5 cells with authentic SARS-CoV-2 and treated with 100 nM halofuginone or vehicle, either before or after infection. Pretreatment with halofuginone alone significantly reduced SARS-CoV-2 infection by ~30-fold (Fig. 6b). Intriguingly, halofuginone added after viral infection reduced the amount of secreted infectious virions by nearly 1000-fold (Fig. 6b). Intracellular viral RNA did not change when the cells were only treated before infection as expected, but viral RNA levels dramatically decreased 10- to 100-fold when halofuginone was present after infection (Fig. 6c). These observations suggest that halofuginone inhibits SARS-CoV-2 post-entry in addition to suppressing HS-dependent infection. These observations were confirmed in the commonly used Vero E6 cells, without affecting cell viability in the effective dose range (**Supplemental Fig. 3e**). Addition of halofuginone post infection inhibited SARS-CoV-2 infectivity as measured by immunofluorescent (IF) detection of the nucleocapsid protein, intracellular viral RNA and plaque assays with an IC_{50} of 13 nM, 34.9 nM, 27.3 nM respectively (Fig. 6d,e). We compared activity of halofuginone with the antiviral, Remdesivir, and tested in parallel these two compounds ability to block viral replication in Vero E6 cells (Fig. 6d). Remdesivir had a calculated IC_{50} of 8 μM, thus halofuginone showed a ~1,000-fold more potent inhibition of infection as compared to Remdesivir in this experimental setup (Fig. 6d). This suggest that halofuginone exerts antiviral effects beyond inhibition of viral attachment mediated by HS.

PRS Targeting Inhibits SARS-CoV-2 Virus Infection Independent of the Integrated Stress Response

Post-infection halofuginone treatment in Vero E6 cells was used to evaluate effects of PRS inhibition on SARS-CoV-2 intra-host replication. The active 2*R*,3*S*-(+) enantiomer inhibited SARS-CoV-2 infectivity with an IC_{50} of 12 nM compared to an IC_{50} of 28 nM for the racemic mixture (Fig.7a). Both the active 2*R*,3*S*-(+) enantiomer and halofuginone did not cause cytotoxicity but did decrease cell proliferation as previously described (**Supplemental Fig. 4a,b and**

Supplemental Table 2) (Pines and Spector, 2015). No inhibition was observed when using the non-PRS targeting 2*S*,3*R*-(-) enantiomer (Fig. 7a and extended Fig. 8). Like halofuginone, the PRS inhibitors ProSA and halofuginol inhibited authentic SARS-CoV-2 infection of Vero E6 cells, although at significantly higher doses (Fig. 7b). The inactive halofuginone derivative, MAZ1310, did not affect infection (Fig. 7b). Proline (4mM) supplementation to the media suppressed the inhibitory activity of halofuginone as demonstrated by a shift in the IC_{50} from 12.5 nM to 210 nM (Fig 7c and **Supplemental Fig. 4c**). Similarly, HS production in Vero E6 cells was negatively impacted by halofuginone treatment in a proline-depended manner (**Supplemental Fig. 4d**). These results collectively demonstrate that halofuginone suppresses SARS-CoV-2 infection post viral entry by competitively inhibiting the PRS.

To further support the hypothesis of SARS-CoV-2 proline translational vulnerability, we tested whether inhibition of other AARS proteins would also inhibit viral replication. Vero E6 cells were treated with either borrelidin, an inhibitor of the threonyl-tRNA synthetase, or seryl-sulfamoyl adenosine (SerSA), an inhibitor of the seryl-tRNA-synthetase (Ho et al., 2018). Neither borrelidin or SerSA were able to significantly attenuate viral replication (Fig. 7d) suggesting that SARS-CoV-2 and possible other RNA viruses, are particular sensitive to proline translation inhibition (Huter et al., 2017; Pavlov et al., 2009).

To test whether activation of the ISR by halofuginone contributed to inhibition of viral replication, we tested inhibitors of the ISR, as well as inhibitors of eIF2-alpha kinases PERK and GCN2 in Vero E6 infection by authentic SARS-CoV-2 virus. Inhibitors of the ISR were unable to attenuate the halofuginone-mediated inhibition of SARS-CoV-2 infectivity (Fig. 7e). Finally, similar to halofuginone, the threonyl-tRNA synthetase inhibitor borrelidin was able to activate the ISR as measured by phosphorylation of eIF2α in Vero E6 (Fig. 7f), while unable to inhibit authentic SARS-CoV-2 infection (Fig. 7d). This was also reflected by equal activation of ISR genes in Vero E6 cells by borrelidin, comparable to the active halofuginone 2*R*,3*S*-(+) enantiomer as determined by RNA-seq (Fig. 7g). Hence, consistent with the effects seen on mAb 10E4 and recombinant

RBD spike protein binding, the observed antiviral effect mediated by HF post-viral entry is independent of ISR activation (Krahling et al., 2009; Nakagawa et al., 2016).

DISCUSSION

In this study, we show that halofuginone is a potent inhibitor of SARS-CoV-2 cellular entry and intra host replication. The treatment with halofuginone in various cell types infected with SARS-CoV-2, including primary human bronchial epithelial cells, inhibited viral infection. We show that halofuginone inhibits the presentation of HS at the cell surface, decreasing spike protein binding, SARS-CoV-2 spike protein pseudo-typed VSV viral infection, and infection by authentic SARS-CoV-2 virus. Interestingly, halofuginone also inhibits authentic SARS-CoV-2 infection post-entry by an HS-independent mechanism. Mechanistically, halofuginone targets the PRS to deplete proline-tRNAs. This has an impact on cell surface HS presentation and SARS-CoV-2 intra-host replication. Interestingly, we observe that particularly HSPGs and SARS-CoV-2 polyproteins required for viral replication are enriched with prolines potentially making them vulnerable to the translational defects caused by proline-tRNA depletion as suggested previously (Wu et al., 2020).

During translation, ribosomes bind to mRNA and incorporate tRNAs to assemble the polypeptide chain. The rate of peptide bond formation is influenced by the chemical properties of each amino acid side chain (Pavlov et al., 2009). In the case of proline-tRNA, proline incorporation is thought to occur at a much slower rate compared to other tRNAs and sequential proline addition may contribute to ribosomal stalling and destabilization of peptidyl-tRNA (Huter et al., 2017; Pavlov et al., 2009). In light of this, we attempted to visualize proline content in HSPGs and SARS-CoV-2 encoded proteins. We observed that many of these proteins are a high in proline content and proline density compared to other proteins. The proline codon enrichment may contribute to translational sensitivity when cells are depleted for proline-tRNA by PRS inhibition using

halofuginone. Targeting the threonyl- or seryl-tRNA synthetases did not decrease SARS-CoV-2 viral infection, suggesting that production of SARS-CoV-2 polyproteins pp1a and pp1ab upon infection is particular vulnerable to proline-tRNA depletion. More studies are needed to determine whether inhibiting other AARS proteins can have a similar effects in inhibiting SARS-CoV-2 replication.

We found proline codon rich polyproteins in most coronaviruses such as SARS-CoV-1, Middle eastern respiratory syndrome (MERS), HCoV-229E, and HCoV-NL63 as well as polymerases observe in other positive sense RNA viruses, such as flaviviruses and alphaviruses. Consistent with this idea, halofuginone demonstrates antiviral activity against future deleterious coronaviruses and other positive ssRNA viruses, including Chikungunya virus, Dengue virus, Zika virus, and Sindbis virus (Hwang et al., 2019). This suggest that beyond SARS-CoV-2, halofuginone may present pan-antiviral activity for other positive sense RNA viruses encoding large proline codon-rich polyproteins. More importantly, it suggest that halofuginone may be a first line treatment for use on future coronaviruses.

There is still today a desperate need for a potent, orally bioavailable antiviral for the treatment of COVID-19 that can be administered early in the disease to prevent hospitalization and the development of severe pulmonary disease. Here, we demonstrate that halofuginone is a potent inhibitor of SARS-CoV-2 infection with IC50 values in the low nanomolar range, in multiple *in vitro* models of infection. Halofuginone is orally bioavailable and reached an average C_{max} of 0.54 ng/ml (~1.3 nM) or 3.09 ng/ml (~7.4 nM) after a single administration of 0.5 mg or 3.5 mg doses in a phase I clinical trial (de Jonge et al., 2006). The long half-life (~30 h) leads to accumulation of halofuginone, with two- to three-fold higher exposure by day 15 of dosing (de Jonge et al., 2006). Halofuginone widely distributed in tissues after administration in mice with the highest tissue concentrations in the lung and kidney (Stecklair et al., 2001). Expressed as area under the curve, halofuginone exposure was more than 87-fold higher in the lung compared to plasma after a single intravenous injection in mice (Stecklair et al., 2001). This suggests that

although it may be difficult to obtain halofuginone plasma levels significantly above the IC_{50} values determined in this study, doses tested in phase I trials may be sufficient to achieve significant anti-SARS-CoV-2 activity in the lung and other organs infected by SARS-CoV-2 (Ackermann et al., 2020; Chan et al., 2020; Gupta et al., 2020; Puelles et al., 2020).

Excessive inflammation can contribute to inflammatory organ injury during severe COVID-19. There are multiple anti-inflammatory agents under evaluation for the treatment of COVID-19 and low dose dexamethasone recently demonstrated lower 28-day mortality in individuals receiving respiratory support (Group et al., 2020). In addition to the antiviral activity against SARS-CoV-2 that is described here, halofuginone has anti-inflammatory and anti-fibrotic activity. Whether this will provide any yet another additive benefit to individuals with COVID-19 pneumonia will need to be determined in future pre-clinical and clinical trials (Battu et al., 2018; Keller et al., 2012; Luo et al., 2018; Luo et al., 2017; Pines and Spector, 2015; Sundrud et al., 2009).

In addition to halofuginone, other PRS inhibitors are being evaluated in humans, including DWN12088 that is in phase I clinical trials in Australia and anticipated to be used for the treatment of interstitial pulmonary fibrosis. Thus, evaluation of PRS inhibitors, halofuginone analogs, and other AARS inhibitors may lead to the identification of additional broad-spectrum antiviral agents.

Viruses require host cell resources for replication and thus can be inhibited by therapeutics that target essential host factors. This approach could provide broad activity against diverse viruses while decreasing the risk of emerging viral resistance as the therapy is not directed against a specific virally encoded product. On the other hand, targeting host factors can lead to cytostatic and cytotoxicity, and we did observe the reported anti-proliferative effect of halofuginone in our assays (Luo et al., 2017). Although inhibition of global translation could lead to excessive toxicity, inhibiting AARS proteins could provide a more precise way of inhibiting viral proteins and thus limit toxicity. It appears that normal cells are relatively tolerant of decreased AARS levels with minimal effects on global translation. Individuals who are heterozygous carriers for recessive

inactivating AARS mutations linked to hypomyelinating leukodystrophy do not display dis ease phenotypes (Kwon et al., 2019).

In conclusion, we identified halofuginone as an antiviral with potent inhibitory activity against SARS-CoV-2 infection in multiple human cell types. We show that halofuginone reduces both HS and HSPG biosynthesis, that are required for viral adhesion. In addition, we find that the inhibitory capacity of halofuginone on SARS-CoV-2 infection is not limited to HS reduction, but also shows potent inhibition in the viral replication stage. Mechanistically, our data suggests that these effects are caused by PRS inhibition and its effect on production of proline-rich proteins and not dependent on ISR activation. This observation is in agreement with previous studies reporting that coronaviruses overcome the inhibitory effects of eIF2α phosphorylation on viral mRNA translation (Krahling et al., 2009; Nakagawa et al., 2016). Furthermore, many viruses, including coronaviruses (SARS1 and SARS2), shutdown host translation using nonstructural protein 1 (Nsp1) and activate eIF2α associated PERK dependent stress responses that benefit the virus (Thoms et al., 2020). Halofuginone may prevent SARS-CoV-2 from circumventing these mechanisms of host protein translational shutdown.

Halofuginone oral administration has been evaluated in a phase I clinical trial in humans and based on pharmacological studies in mice is distributed to SARS-CoV-2 target organs, including the lung. However, further distribution, safety and tolerability assessments are required in humans for oral or intranasal applications. In conclusion, we show that halofuginone is a potent inhibitor of SARS-CoV-2 infection which emphasizes its potential as an effective treatment for COVID-19 in the clinic. Beyond its antiviral activity, halofuginone has potent anti-inflammatory and anti-fibrotic properties that may provide additive benefit in the treatment of COVID-19 pneumonia. Based on this in vitro preclinical data we believe halofuginone could be an effective antiviral agent for the treatment of individuals with COVID-19.

ACKNOWLEDGMENTS

We thank John Christianson, University of Oxford, and Matthew Frieman at the University of Maryland for discussions and helpful comments, and Alexandra Efstrathiou, University of Oxford, for technical assistance. This work was supported by Foundation Leducq 16CVD01 to P.L.S.M.G., U.O., R.M.E. and S.T., a UCSD Innovation Grant 13991 to P.L.S.M.G., a RAPID grant 2031989 from the National Science Foundation and Project 3 of NIH P01 HL131474 to J.D.E.; The Alfred Benzon Foundation to T.M.C; NIH grant 5T32GM127235-02 to J.K.C.C.; NIH fellowship support K12HL141956 to R.J.W.; The Carlsberg Foundation Fellowship to K.V.G.; a Career Award for Medical Scientists from the Burroughs Wellcome Fund to A.F.C. NIH Grant R01 HL124209, the American Asthma Foundation, and the BSF 2017176 to B.A.C.; COVID19 seed funding from the Huck Institutes of the Life Sciences and Penn State start-up funds to J.J.; R.M. NIH 1R21AI132981-01, the Bill and Melinda Gates Foundation OPP1086203 and Cancer Research UK and Arthritis Research UK 20522 grants to U.O.

AUTHOR CONTRIBUTIONS

P.L.S.M.G., A.F.C., D.R.S., T.M.C. and C.N. conceived the project; P.L.S.M.G., A.F.C., J.D.E., J.J., S.T., B.A.C., S.L., R.M., B.A.C., K.Z., U.O., D.R.S., T.M.C., R.J. W., J.M., and C.N designed and performed the experimental work.; A.D., A.P.C., A.E.C., A.F.G, J.K.C.K., A.N., S.A.M., G.J.G., C.B.S, C.J.N., E.R.G., J.E.D, C.J.N, E.R.G, E.M.K., R.N.M. and A.P. performed the experimental work.: X.Y., Y.P., J.F., B.H., T.M.C., S.K.C., M.A.T., N.C.P, A.G.S. J.A.M., T.A., C.B, M.D., R.M.E. and R.M. supplied reagents. P.L.S.M.G., A.F.C. D.R.S., T.M.C., J.K.C.K., J.D.E., U.O., R.M., J.A.M., M.D., R.M.E., A.P.C., M.P, C.J., B.A.C., K.V.G. and S.T. analyzed and discussed the data.; T.M.C., D.R.S., A.F.C. and P.L.S.M.G, wrote the manuscript. All authors discussed the experiments and results, read, and approved the manuscript.

DECLARATION OF INTERESTS

S.T. is a founding member of Oxitope, Inc, and Kleanthi Diagnostics. S.T. is a consultant for Ionis Pharmaceuticals. The other authors declare that they have no competing interests. J.D.E. is a co-founder of TEGA Therapeutics. J.D.E. and The Regents of the University of California have licensed a University invention to and have an equity interest in TEGA Therapeutics. The terms of this arrangement have been reviewed and approved by the University of California, San Diego in accordance with its conflict of interest policies. NIH R01 AI146779 and a Massachusetts Consortium on Pathogenesis Readiness (MassCPR) grant to A.G.S.; training grants: NIGMS T32 GM007753 for B.M.H. and T.M.C; T32 AI007245 for J.F. R.M. is a scientific advisory board (SAB) member and equity holder of Regenacy Pharmaceuticals, ERX Pharmaceuticals, Frequency Therapeutics. R.M., M.A.T. and N.C.P. are inventors on patent applications related to PRS inhibitors.

REFERENCES

(2020a). Food and Drug Administration. https://www.fda.gov/news-events/press-announcements/coronavirus-covid-19-update-fda-issues-emergency-use-authorization-potential-covid-19-treatment.

(2020b). Johns Hopkins University and Medicine, Johns Hopkins Coronavirus Resource Centre. https://coronavirus.jhu.edu.

Ackermann, M., Verleden, S.E., Kuehnel, M., Haverich, A., Welte, T., Laenger, F., Vanstapel, A., Werlein, C., Stark, H., Tzankov, A., et al. (2020). Pulmonary Vascular Endothelialitis, Thrombosis, and Angiogenesis in Covid-19. N Engl J Med 383, 120-128.

Adachi, R., Okada, K., Skene, R., Ogawa, K., Miwa, M., Tsuchinaga, K., Ohkubo, S., Henta, T., and Kawamoto, T. (2017). Discovery of a novel prolyl-tRNA synthetase inhibitor and elucidation of its binding mode to the ATP site in complex with l-proline. Biochem Biophys Res Commun 488, 393-399.

Anower, E.K.F., Singh, G., Deng, Y., Gordts, P., and Esko, J.D. (2020). Corrigendum to: Triglyceride-rich lipoprotein binding and uptake by heparan sulfate proteoglycan receptors in a CRISPR/Cas9 library of Hep3B mutants. Glycobiology 30, 760.

Battu, S., Afroz, S., Giddaluru, J., Naz, S., Huang, W., Khumukcham, S.S., Khan, R.A., Bhat, S.Y., Qureshi, I.A., Manavathi, B., et al. (2018). Amino acid starvation sensing dampens IL-1beta production by activating riboclustering and autophagy. PLoS Biol 16, e2005317.

Beigel, J.H., Tomashek, K.M., Dodd, L.E., Mehta, A.K., Zingman, B.S., Kalil, A.C., Hohmann, E., Chu, H.Y., Luetkemeyer, A., Kline, S., et al. (2020). Remdesivir for the Treatment of Covid-19 - Preliminary Report. N Engl J Med.

Blight, K.J., McKeating, J.A., and Rice, C.M. (2002). Highly permissive cell lines for subgenomic and genomic hepatitis C virus RNA replication. J Virol 76, 13001-13014.

Chan, J.F., Zhang, A.J., Yuan, S., Poon, V.K., Chan, C.C., Lee, A.C., Chan, W.M., Fan, Z., Tsoi, H.W., Wen, L., et al. (2020). Simulation of the clinical and pathological manifestations of Coronavirus Disease 2019 (COVID-19) in golden Syrian hamster model: implications for disease pathogenesis and transmissibility. Clin Infect Dis.

Clausen, T.M., Sandoval, D.R., Spliid, C.B., Pihl, J., Painter, C.D., Thacker, B.E., Glass, C.A., Narayanan, A., Majowicz, S.A., Zhang, Y., et al. (2020). SARS-CoV-2 Infection Depends on Cellular Heparan Sulfate and ACE2. Cell.

Costa-Mattioli, M., and Walter, P. (2020). The integrated stress response: From mechanism to disease. Science 368.

Cottone, L., Cribbs, A.P., Khandelwal, G., Wells, G., Ligammari, L., Philpott, M., Tumber, A., Lombard, P., Hookway, E.S., Szommer, T., et al. (2020). Inhibition of histone H3K27 demethylases inactivates brachyury (TBXT) and promotes chordoma cell death. Cancer Res.

Cribbs, A., Hookway, E.S., Wells, G., Lindow, M., Obad, S., Oerum, H., Prinjha, R.K., Athanasou, N., Sowman, A., Philpott, M., et al. (2018). Inhibition of histone H3K27 demethylases selectively modulates inflammatory phenotypes of natural killer cells. J Biol Chem 293, 2422-2437.

Cribbs AP, L.-V.S., George C et al. (2019). CGAT-core: a python framework for building scalable, reproducible computational biology workflows. F1000Research 8:377.

Cribbs, A.P., Terlecki-Zaniewicz, S., Philpott, M., Baardman, J., Ahern, D., Lindow, M., Obad, S., Oerum, H., Sampey, B., Mander, P.K., et al. (2020). Histone H3K27me3 demethylases regulate human Th17 cell development and effector functions by impacting on metabolism. Proc Natl Acad Sci U S A 117, 6056-6066.

David, G., Bai, X.M., Van der Schueren, B., Cassiman, J.J., and Van den Berghe, H. (1992). Developmental changes in heparan sulfate expression: in situ detection with mAbs. J Cell Biol 119, 961-975.

de Jonge, M.J., Dumez, H., Verweij, J., Yarkoni, S., Snyder, D., Lacombe, D., Marreaud, S., Yamaguchi, T., Punt, C.J., van Oosterom, A., et al. (2006). Phase I and pharmacokinetic study of halofuginone, an oral quinazolinone derivative in patients with advanced solid tumours. Eur J Cancer 42, 1768-1774.

Duin, R.P.W. (1976). On the choice of smoothing parameters of Parzen estimators of probability density functions. . IEEE Transactions on Computers C-25, 1175–1179.

Esko, J.D. (1993). Special considerations for proteoglycans and glycosaminoglycans and their purification. In Current protocols in molecular biology. F. Ausubel, R. Brent, B. Kingston, D. Moore, J. Seidman, J. Smith, K. Struhl, A. Varki, and J. Coligan, eds. (New York: Greene Publishing and Wiley-Interscience), pp. 17.12.11-17.12.19.

Francklyn, C.S., and Mullen, P. (2019). Progress and challenges in aminoacyl-tRNA synthetase-based therapeutics. J Biol Chem 294, 5365-5385.

Fusakio, M.E., Willy, J.A., Wang, Y., Mirek, E.T., Al Baghdadi, R.J., Adams, C.M., Anthony, T.G., and Wek, R.C. (2016). Transcription factor ATF4 directs basal and stress-induced gene expression in the unfolded protein response and cholesterol metabolism in the liver. Mol Biol Cell 27, 1536-1551.

Gordon, D.E., Jang, G.M., Bouhaddou, M., Xu, J., Obernier, K., White, K.M., O'Meara, M.J., Rezelj, V.V., Guo, J.Z., Swaney, D.L., et al. (2020). A SARS-CoV-2 protein interaction map reveals targets for drug repurposing. Nature 583, 459-468.

Gordts, P., Foley, E.M., Lawrence, R., Sinha, R., Lameda-Diaz, C., Deng, L., Nock, R., Glass, C.K., Erbilgin, A., Lusis, A.J., et al. (2014). Reducing macrophage proteoglycan sulfation increases atherosclerosis and obesity through enhanced type I interferon signaling. Cell Metab 20, 813-826.

Group, R.C., Horby, P., Lim, W.S., Emberson, J.R., Mafham, M., Bell, J.L., Linsell, L., Staplin, N., Brightling, C., Ustianowski, A., et al. (2020). Dexamethasone in Hospitalized Patients with Covid-19 - Preliminary Report. N Engl J Med.

Guidoum, A.C. (2015). kedd: Kernel estimator and bandwidth selection for density and its derivatives. R. Package version 1.0.3. http://CRAN.R-project.org/package=kedd.

Gupta, A., Madhavan, M.V., Sehgal, K., Nair, N., Mahajan, S., Sehrawat, T.S., Bikdeli, B., Ahluwalia, N., Ausiello, J.C., Wan, E.Y., et al. (2020). Extrapulmonary manifestations of COVID-19. Nat Med 26, 1017-1032.

H. Wickham, R.F., L. Henry, K. Müller (2020). dplyr: A Grammar of Data Manipulation. R package version 0.8. https://CRAN.R-project.org/package=dplyr.

Heinz, S., Benner, C., Spann, N., Bertolino, E., Lin, Y.C., Laslo, P., Cheng, J.X., Murre, C., Singh, H., and Glass, C.K. (2010). Simple combinations of lineage-determining transcription factors prime cis-regulatory elements required for macrophage and B cell identities. Mol Cell 38, 576-589.

Herman, J.D., Pepper, L.R., Cortese, J.F., Estiu, G., Galinsky, K., Zuzarte-Luis, V., Derbyshire, E.R., Ribacke, U., Lukens, A.K., Santos, S.A., et al. (2015). The cytoplasmic prolyl-tRNA synthetase of the malaria parasite is a dual-stage target of febrifugine and its analogs. Sci Transl Med 7, 288ra277.

Hie, B., Zhong, E.D., Berger, B., and Bryson, B. (2021). Learning the language of viral evolution and escape. Science 371, 284-288.

Ho, J.M., Bakkalbasi, E., Soll, D., and Miller, C.A. (2018). Drugging tRNA aminoacylation. RNA Biol 15, 667-677.

Hoffmann, M., Kleine-Weber, H., Schroeder, S., Kruger, N., Herrler, T., Erichsen, S., Schiergens, T.S., Herrler, G., Wu, N.H., Nitsche, A., et al. (2020). SARS-CoV-2 Cell Entry Depends on ACE2 and TMPRSS2 and Is Blocked by a Clinically Proven Protease Inhibitor. Cell 181, 271-280 e278.

Huter, P., Arenz, S., Bock, L.V., Graf, M., Frister, J.O., Heuer, A., Peil, L., Starosta, A.L., Wohlgemuth, I., Peske, F., et al. (2017). Structural Basis for Polyproline-Mediated Ribosome Stalling and Rescue by the Translation Elongation Factor EF-P. Mol Cell 68, 515-527 e516.

Hwang, J., Jiang, A., and Fikrig, E. (2019). A potent prolyl tRNA synthetase inhibitor antagonizes Chikungunya and Dengue viruses. Antiviral Res 161, 163-168.

J.D.F. Habbema, J.H., and K. Van den Broek (1974). A stepwise discrimination analysis program using density estimation. Compstat 1974: Proceedings in Computational Statistics, Physica Verlag, Vienna.

Jain, V., Yogavel, M., Oshima, Y., Kikuchi, H., Touquet, B., Hakimi, M.A., and Sharma, A. (2015). Structure of Prolyl-tRNA Synthetase-Halofuginone Complex Provides Basis for Development of Drugs against Malaria and Toxoplasmosis. Structure 23, 819-829.

Jose, J., Taylor, A.B., and Kuhn, R.J. (2017). Spatial and Temporal Analysis of Alphavirus Replication and Assembly in Mammalian and Mosquito Cells. mBio 8.

Kamtekar, S., Kennedy, W.D., Wang, J., Stathopoulos, C., Soll, D., and Steitz, T.A. (2003). The structural basis of cysteine aminoacylation of tRNAPro by prolyl-tRNA synthetases. Proc Natl Acad Sci U S A 100, 1673-1678.

Kassambara, A. (2020). ggpubr: 'ggplot2' Based Publication Ready Plots. Package version 0.4.0. https://CRAN.R-project.org/package=ggpubr.

Keller, T.L., Zocco, D., Sundrud, M.S., Hendrick, M., Edenius, M., Yum, J., Kim, Y.J., Lee, H.K., Cortese, J.F., Wirth, D.F., et al. (2012). Halofuginone and other febrifugine derivatives inhibit prolyl-tRNA synthetase. Nat Chem Biol 8, 311-317.

Kim, D., Paggi, J.M., Park, C., Bennett, C., and Salzberg, S.L. (2019). Graph-based genome alignment and genotyping with HISAT2 and HISAT-genotype. Nat Biotechnol 37, 907-915.

Krahling, V., Stein, D.A., Spiegel, M., Weber, F., and Muhlberger, E. (2009). Severe acute respiratory syndrome coronavirus triggers apoptosis via protein kinase R but is resistant to its antiviral activity. J Virol 83, 2298-2309.

Kwon, N.H., Fox, P.L., and Kim, S. (2019). Aminoacyl-tRNA synthetases as therapeutic targets. Nat Rev Drug Discov 18, 629-650.

Lawrence, R., Olson, S.K., Steele, R.E., Wang, L., Warrior, R., Cummings, R.D., and Esko, J.D. (2008). Evolutionary differences in glycosaminoglycan fine structure detected by quantitative glycan reductive isotope labeling. J Biol Chem 283, 33674-33684.

Liao, Y., Smyth, G.K., and Shi, W. (2019). The R package Rsubread is easier, faster, cheaper and better for alignment and quantification of RNA sequencing reads. Nucleic Acids Res 47, e47.

Luo, L., Gao, Y., Yang, C., Shao, Z., Wu, X., Li, S., Xiong, L., and Chen, C. (2018). Halofuginone attenuates intervertebral discs degeneration by suppressing collagen I production and inactivating TGFbeta and NF-small ka, CyrillicB pathway. Biomed Pharmacother 101, 745-753.

Luo, Y., Xie, X., Luo, D., Wang, Y., and Gao, Y. (2017). The role of halofuginone in fibrosis: more to be explored? J Leukoc Biol 102, 1333-1345.

McCreary, E.K., and Angus, D.C. (2020). Efficacy of Remdesivir in COVID-19. JAMA.

Mycroft-West, C.J., Su, D., Pagani, I., Rudd, T.R., Elli, S., Guimond, S.E., Miller, G., Meneghetti, M.C.Z., Nader, H.B., Li, Y., et al. (2020). Heparin inhibits cellular invasion by SARS-CoV-2: structural dependence of the interaction of the surface protein (spike) S1 receptor binding domain with heparin. bioRxiv, 2020.2004.2028.066761.

Nakagawa, K., Lokugamage, K.G., and Makino, S. (2016). Viral and Cellular mRNA Translation in Coronavirus-Infected Cells. Adv Virus Res 96, 165-192.

Nakamura, A., Nambu, T., Ebara, S., Hasegawa, Y., Toyoshima, K., Tsuchiya, Y., Tomita, D., Fujimoto, J., Kurasawa, O., Takahara, C., et al. (2018). Inhibition of GCN2 sensitizes ASNS-low cancer cells to asparaginase by disrupting the amino acid response. Proc Natl Acad Sci U S A 115, E7776-E7785.

Pavlov, M.Y., Watts, R.E., Tan, Z., Cornish, V.W., Ehrenberg, M., and Forster, A.C. (2009). Slow peptide bond formation by proline and other N-alkylamino acids in translation. Proc Natl Acad Sci U S A 106, 50-54.

Pessentheiner, A.R., Ducasa, G.M., and Gordts, P. (2020). Proteoglycans in Obesity-Associated Metabolic Dysfunction and Meta-Inflammation. Front Immunol 11, 769.

Pines, M., and Spector, I. (2015). Halofuginone - the multifaceted molecule. Molecules 20, 573-594.

Puelles, V.G., Lutgehetmann, M., Lindenmeyer, M.T., Sperhake, J.P., Wong, M.N., Allweiss, L., Chilla, S., Heinemann, A., Wanner, N., Liu, S., et al. (2020). Multiorgan and Renal Tropism of SARS-CoV-2. N Engl J Med 383, 590-592.

Sarrazin, S., Lamanna, W.C., and Esko, J.D. (2011). Heparan sulfate proteoglycans. Cold Spring Harb Perspect Biol 3.

Schwarz, M.C., Sourisseau, M., Espino, M.M., Gray, E.S., Chambers, M.T., Tortorella, D., and Evans, M.J. (2016). Rescue of the 1947 Zika Virus Prototype Strain with a Cytomegalovirus Promoter-Driven cDNA Clone. mSphere 1.

Sims, D., Ilott, N.E., Sansom, S.N., Sudbery, I.M., Johnson, J.S., Fawcett, K.A., Berlanga-Taylor, A.J., Luna-Valero, S., Ponting, C.P., and Heger, A. (2014). CGAT: computational genomics analysis toolkit. Bioinformatics 30, 1290-1291.

Son, J., Lee, E.H., Park, M., Kim, J.H., Kim, J., Kim, S., Jeon, Y.H., and Hwang, K.Y. (2013). Conformational changes in human prolyl-tRNA synthetase upon binding of the substrates proline and ATP and the inhibitor halofuginone. Acta Crystallogr D Biol Crystallogr 69, 2136-2145.

Song, Y., Zhou, H., Vo, M.N., Shi, Y., Nawaz, M.H., Vargas-Rodriguez, O., Diedrich, J.K., Yates, J.R., Kishi, S., Musier-Forsyth, K., et al. (2017). Double mimicry evades tRNA synthetase editing by toxic vegetable-sourced non-proteinogenic amino acid. Nat Commun 8, 2281.

Spinner, C.D., Gottlieb, R.L., Criner, G.J., Arribas Lopez, J.R., Cattelan, A.M., Soriano Viladomiu, A., Ogbuagu, O., Malhotra, P., Mullane, K.M., Castagna, A., et al. (2020). Effect of Remdesivir vs Standard Care on Clinical Status at 11 Days in Patients With Moderate COVID-19: A Randomized Clinical Trial. JAMA.

Stecklair, K.P., Hamburger, D.R., Egorin, M.J., Parise, R.A., Covey, J.M., and Eiseman, J.L. (2001). Pharmacokinetics and tissue distribution of halofuginone (NSC 713205) in CD2F1 mice and Fischer 344 rats. Cancer Chemother Pharmacol 48, 375-382.

Sundrud, M.S., Koralov, S.B., Feuerer, M., Calado, D.P., Kozhaya, A.E., Rhule-Smith, A., Lefebvre, R.E., Unutmaz, D., Mazitschek, R., Waldner, H., et al. (2009). Halofuginone inhibits TH17 cell differentiation by activating the amino acid starvation response. Science 324, 1334-1338.

Team, R.C. (2019). R: A language and environment for statistical computing. . R Foundation for Statistical Computing, Vienna, Austria.

Thoms, M., Buschauer, R., Ameismeier, M., Koepke, L., Denk, T., Hirschenberger, M., Kratzat, H., Hayn, M., Mackens-Kiani, T., Cheng, J., et al. (2020). Structural basis for translational shutdown and immune evasion by the Nsp1 protein of SARS-CoV-2. Science.

Thorp, H.H. (2020). A dangerous rush for vaccines. Science 369, 885.

UniProt, C. (2019). UniProt: a worldwide hub of protein knowledge. Nucleic Acids Res 47, D506-D515.

Wang, Y., Zhang, D., Du, G., Du, R., Zhao, J., Jin, Y., Fu, S., Gao, L., Cheng, Z., Lu, Q., et al. (2020). Remdesivir in adults with severe COVID-19: a randomised, double-blind, placebo-controlled, multicentre trial. Lancet 395, 1569-1578.

Whitt, M.A. (2010). Generation of VSV pseudotypes using recombinant DeltaG-VSV for studies on virus entry, identification of entry inhibitors, and immune responses to vaccines. J Virol Methods 169, 365-374.

Wickham, H. (2016). ggplot2: Elegant Graphics for Data Analysis. Springer-Verlag New York. ISBN 978-3-319-24277-4, https://ggplot2.tidyverse.org

Wickham, H. (2019). stringr: Simple, Consistent Wrappers for Common String Operations. R package version 1.4.0. https://CRAN.R-project.org/package=stringr.

Wickham, H. (2020). tidyr: Tidy Messy Data. R package version 1.1.2. https://CRAN.R-project.org/package=tidyr.

Wu, J., Subbaiah, K.C.V., Xie, L.H., Jiang, F., Khor, E.S., Mickelsen, D.M., Myers, J.R., Tang, W.W., and Yao, P. (2020). Glutamyl-Prolyl-tRNA Synthetase Regulates Proline-Rich Pro-fibrotic Protein Synthesis During Cardiac Fibrosis. Circ Res.

Xu, D., and Esko, J.D. (2014). Demystifying heparan sulfate-protein interactions. Annu Rev Biochem 83, 129-157.

Zhou, H., Sun, L., Yang, X.L., and Schimmel, P. (2013). ATP-directed capture of bioactive herbal-based medicine on human tRNA synthetase. Nature 494, 121-124.

Zhou, Y., Zhou, B., Pache, L., Chang, M., Khodabakhshi, A.H., Tanaseichuk, O., Benner, C., and Chanda, S.K. (2019). Metascape provides a biologist-oriented resource for the analysis of systems-level datasets. Nat Commun 10, 1523.

FIGURES AND FIGURE LEGENDS

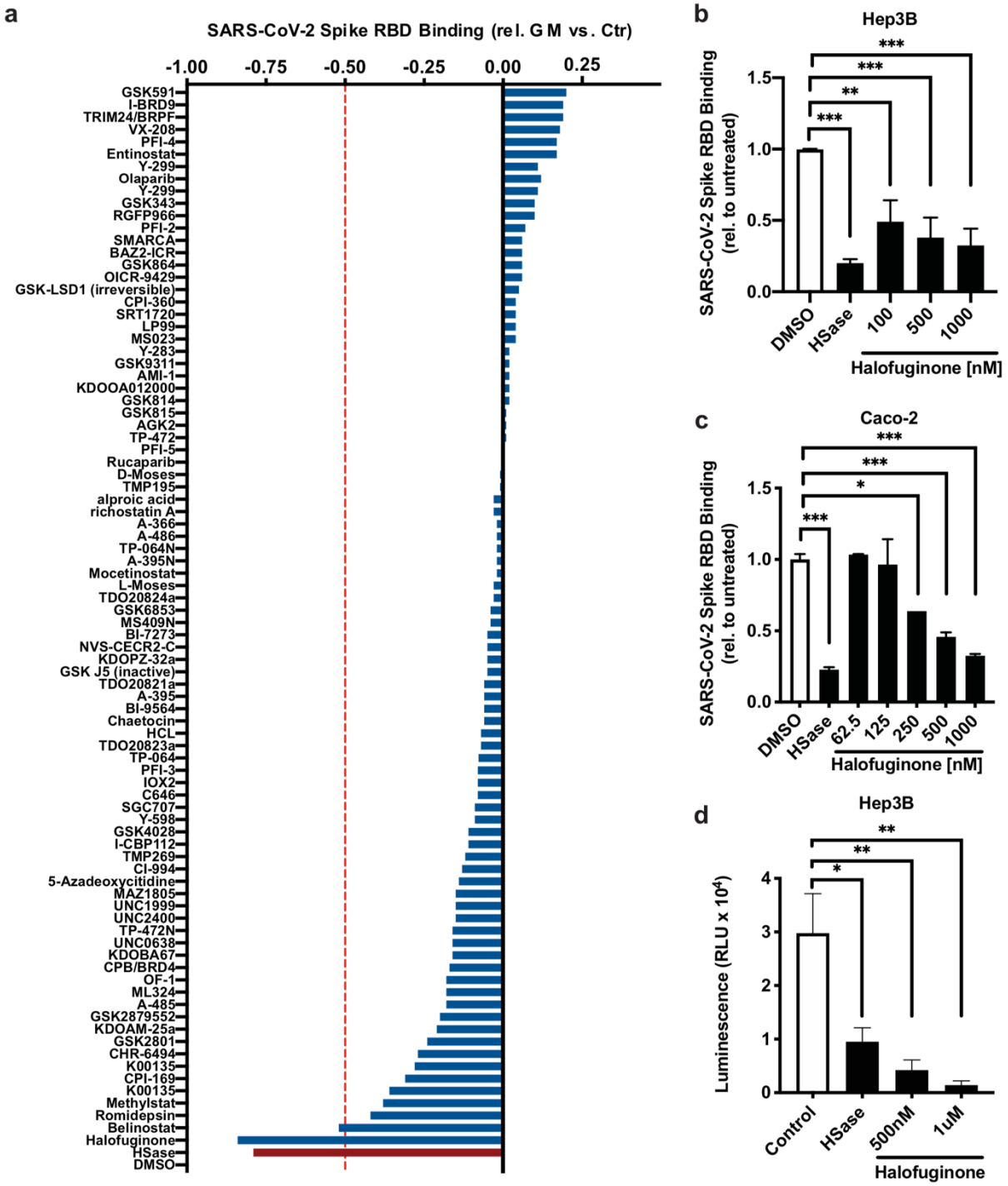

Figure 1. Screen of epigenetic and translational regulatory compounds identify halofuginone as a potent inhibitor of SARS-CoV-2 Spike protein and pseudovirus binding. **a,** Hep3B cells were treated with a library of epigenetic and translational regulatory compounds

or heparin lyase (HSase) as a positive control and tested for their interaction with recombinant SARS-CoV-2 RBD protein. **b-c**, Titration of halofuginone on Hep3B (**b**) and Cacu-2 (**c**) cells and its effect on binding of recombinant SARS-CoV-2 RBD protein (n = 3-4 replicates per condition). **d**, Effect of halofuginone treatment on the infection of SARS-CoV-2 spike protein pseudotyped VSV virus in Hep3B cells (n= 3-4 replicates per condition). Data shown as mean ± S.D. Statistics performed by 1-way ANOVA and uncorrected Fisher's LSD test (ns: $p > 0.05$, *: $p \leq 0.05$, **: $p \leq 0.01$, ***: $p \leq 0.001$).

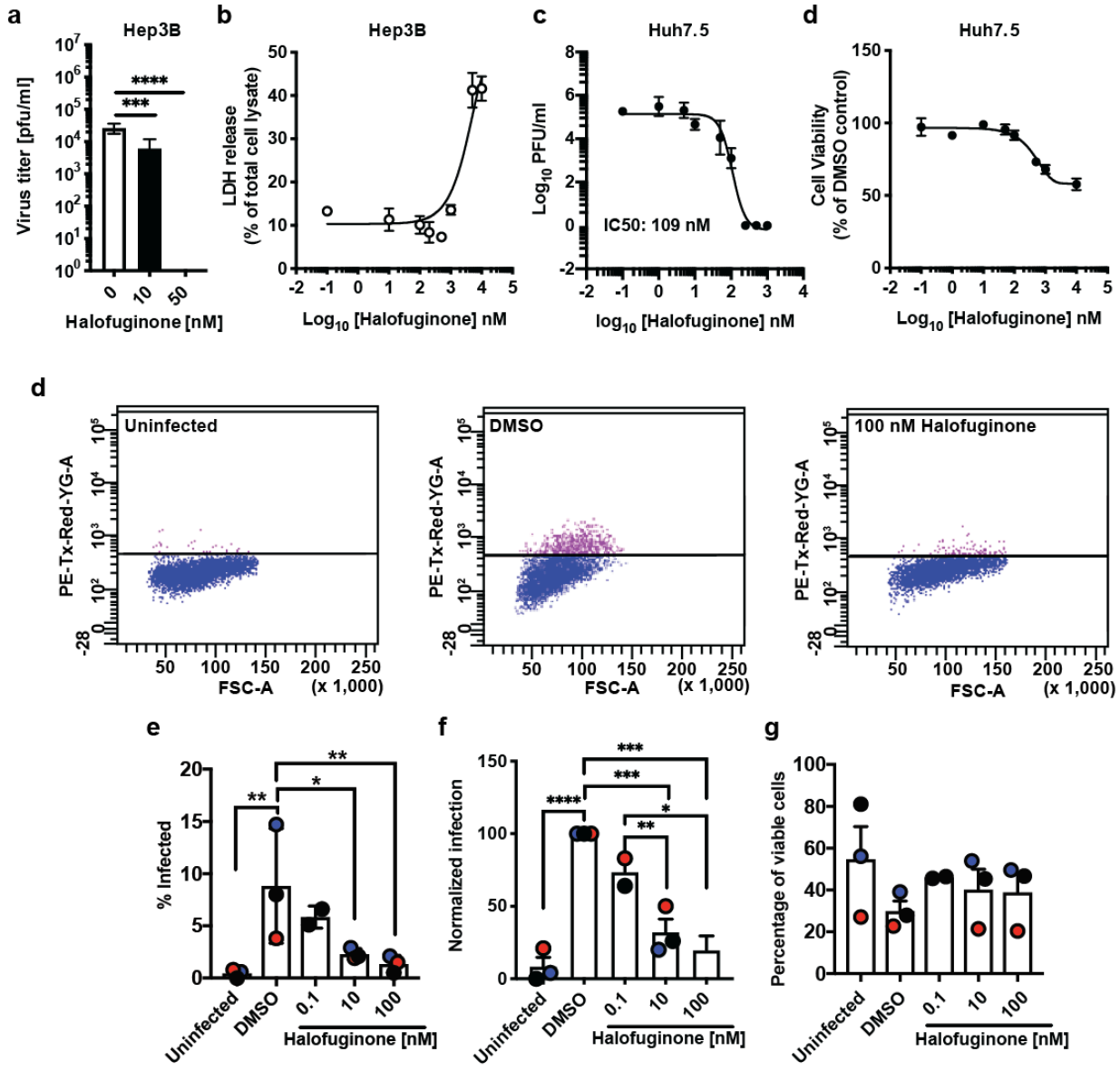

Figure 2. Halofuginone inhibits infection of authentic SARS-COV-2 virus. a, Authentic SARS-CoV-2 virus infection of Hep3B cells treated with halofuginone. **b**, Cell viability in Hep3B cells at indicated concentrations of halofuginone after a 24 hr treatment was measured by lactate dehydrogenase (LDH) release in medium (n =3 per dose). **c**, Authentic SARS-CoV-2 virus infection of HuH7.5 cells treated with halofuginone. **d**, Cell viability was measured using alamarBlue staining in HuH 7.5 cells at indicated concentrations of halofuginone after a 24 hr treatment (n =3 per dose).**c,** Flow cytometry analysis for SARS-CoV-2 Viral nucleocapsid

(conjugated to Alexa594) of primary human airway lung epithelial cells uninfected and infected with SARS-CoV-2 and treated with DMSO or 100 nM halofuginone. **e-f,** Absolute (**e**) and normalized (**f**) percentage of infection with authentic SARS-CoV-2 of human bronchial epithelial cells, grown at an air-liquid interface, treated with Halofuginone as measured by flow cytometry. (Red and black colors represent the two different primary human bronchial epithelial cells isolates used**). d,** Relative cell viability of primary human bronchial epithelial cells. Data shown as mean ± S.D. Statistics performed by 1-way ANOVA and uncorrected Fisher's LSD test (ns: $p > 0.05$, *: $p \leq 0.05$, **: $p \leq 0.01$, ***: $p \leq 0.001$).

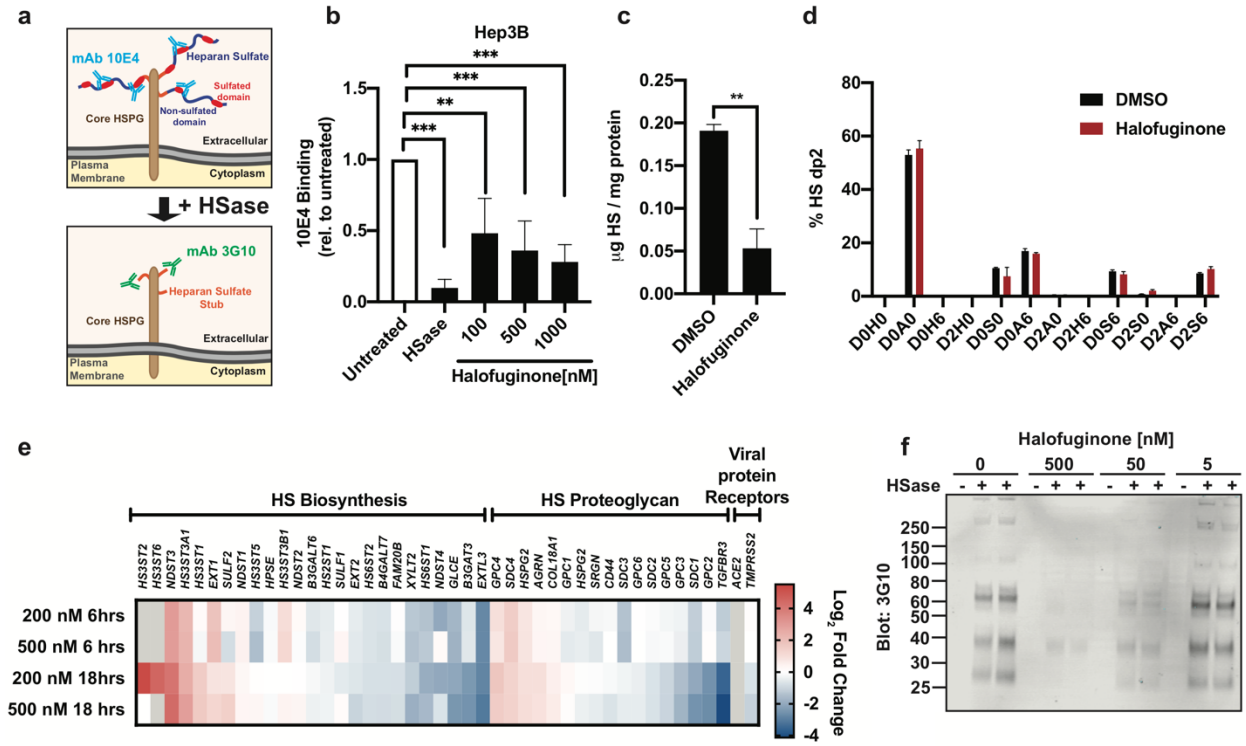

Figure 3. Halofuginone Inhibits Heparan Sulfate Biosynthesis. a,10E4 recognizes sulfated HS polymer, while 3G10 recognizes the number of HS attachments sites by interacting with the stub left after heparin lyase (HSase) treatment. **b,** Titration of halofuginone on Hep3B cells and its effect on 10E4 binding (n = 3 per group). **c,** quantitative determination of HS content in Hep3B cells treated with halofuginone. Absolute HS content was determined by disaccharide analysis using LC-MS (n = 3 per group). **d,** Qualitative distribution of specific sulfation patterns in Hep3B cells treated with halofuginone, seen in the LC-MS analysis (n = 3 per group). **e,** RNA-sequencing of time and dose dependent effects of Halofuginone treatment on expression of HS related biosynthetic enzymes, HSPG core proteins, and sulfate transporters in Hep3b. **f,** Quantification of functional HS binding sites in Hep3B cells treated with halofuginone. Binding sites are quantified in SDS-PAGE using mAb 3G10 that recognizes the linker tetrasaccharide bound to the HSPG core protein after hep lyase treatment. Data shown as mean ± S.D. Statistics performed by unpaired t test or 1-way ANOVA and uncorrected Fisher's LSD test (ns: $p > 0.05$, *: $p \leq 0.05$, **: $p \leq 0.01$, ***: $p \leq 0.001$, ****: $p \leq 0.0001$).

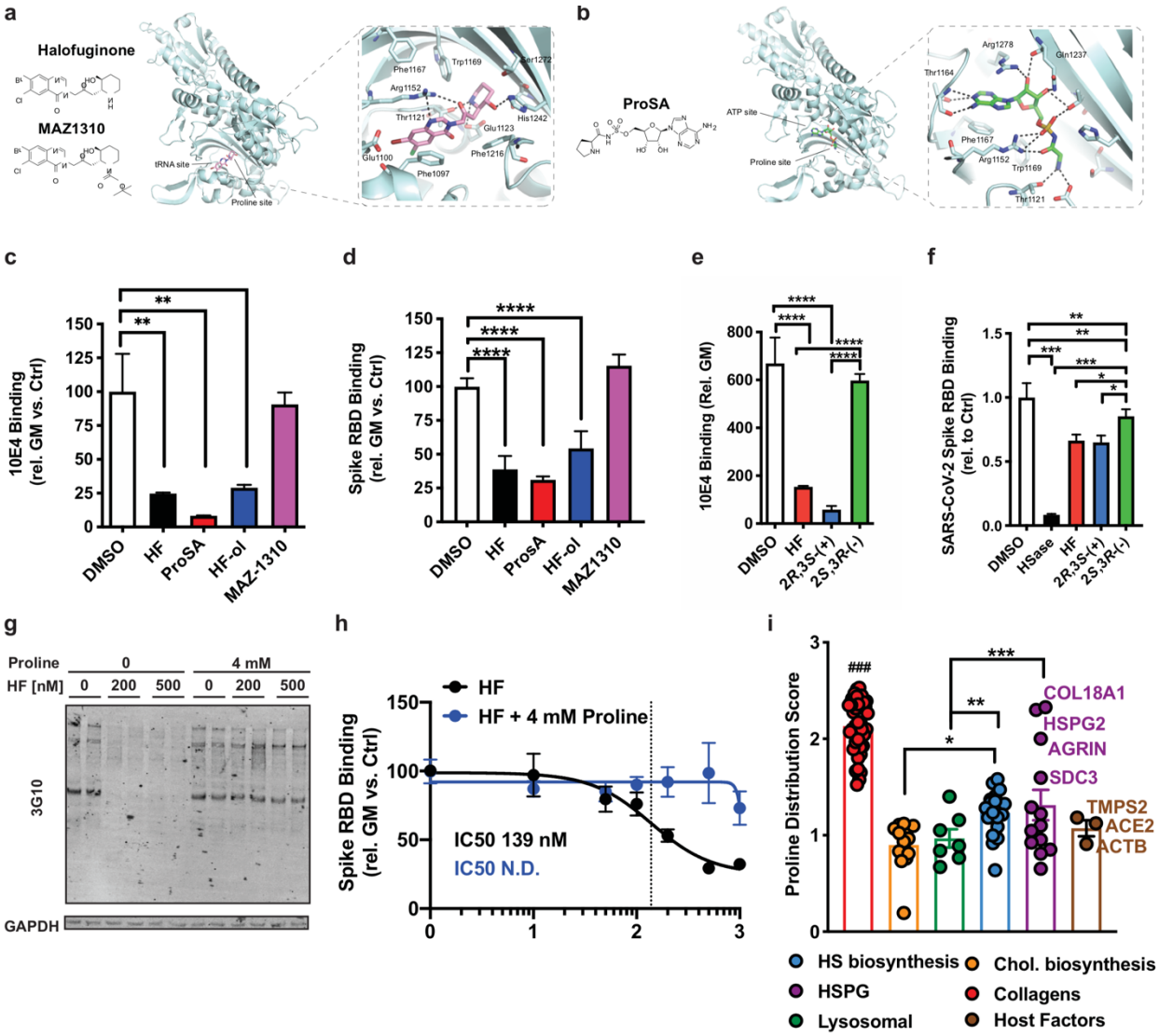

Figure 4. Halofuginone Inhibition of heparan sulfate presentation and Spike protein binding dependents on PRS targeting. a, Chemical structure of halofuginone and negative control compound MAZ1310. Figure shows the interaction of halofuginone with the human prolyl-tRNA synthetase (PRS) active site, as resolved by X-ray crystallography (PDB: 4K88)(Son et al., 2013). **b,** Chemical structure of ProSA. Graphic shows the interaction of ProSA with human PRS (PDB: 5V58)(Song et al., 2017). **c-d,** Treatment of Hep3B cells with modulators of the PRS pathway at 0.5 μM (ProSA at 5 μM) and its effect on (**c**) HS presentation as measured by anti-HS mAb 10E4 binding and (**d**) spike RBD binding by flow cytometry. Binding is represented as relative to non-treated control. **e-f,** Effect of 500 nM halofuginone and 500 nM of the HF enantiomers

2*R*,3*S*-(+) and 2*S*,3*R*-(-) on Hep3B and its effect on cellular staining with (**e**) anti-HS 10E4 mAb or (**f**) SARS-CoV-2 spike RBD protein binding. **g,** Quantification of functional HS binding sites via 3G10 blotting in Hep3B cells treated with halofuginone in the presence or absence of 4mM proline. **h,** Treatment of Hep3B cells with halofuginone in the presence or absence of 4mM proline and its effect on spike RBD binding by flow cytometry. Binding is represented as relative to non-treated control. **i,** The distribution of proline distribution and density depicted as a proline distribution score for collagens, cholesterol biosynthetic proteins, lysosomal proteins, heparan sulfate (HS) biosynthetic proteins, heparan sulfate proteoglycans (HSPG) and viral host factor proteins ($^{\#\#}p \leq 0.01$ collagens vs. all other protein classes). Data shown as mean ± S.D. Statistics performed by 1-way ANOVA and uncorrected Fisher's LSD test (ns: $p > 0.05$, *: $p \leq 0.05$, **: $p \leq 0.01$, ***: $p \leq 0.001$, ****: $p \leq 0.0001$; $^{\#}$:$p \leq 0.05$, $^{\#\#}$: $p \leq 0.01$).

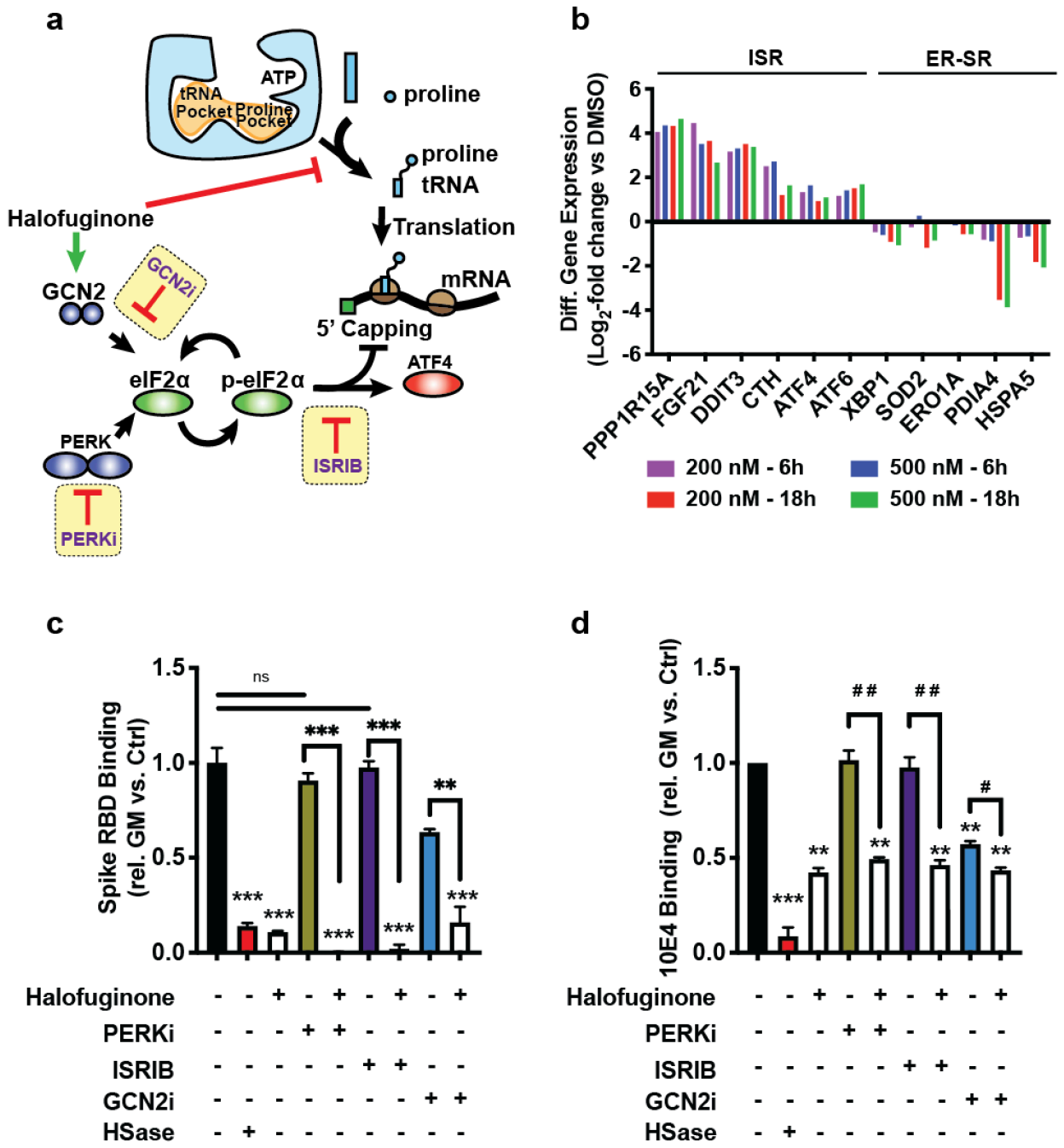

Figure 5. Halofuginone Inhibition of heparan sulfate presentation and Spike protein binding is independent of the integrated stress response. a, Schematic representation of the mediators of the integrated stress response (ISR). **b,** RNA-Seq quantification of genes involved in the ATF4-mediated integrated stress response (ISR) versus genes affected by the ER stress response (ER-SR) upon treatment with Halofuginone (HF) (average of n = 3 per group). **c,**

Treatment of Hep3B cells with modulators of the ISR and its effect on HS presentation as measured by anti-HS mAb 10E4 binding in flow cytometry. **d**, Treatment of Hep3B cells with modulators of the ISR and its effect on SARS-CoV-2 recombinant RBD protein binding in flow cytometry. Binding is represented as relative to non-treated control. Data shown as mean ± S.D. Statistics performed by 1-way ANOVA and uncorrected Fisher's LSD test (ns: $p > 0.05$, *: $p \leq 0.05$, **: $p \leq 0.01$, ***: $p \leq 0.001$, ****: $p \leq 0.0001$; $^{\#}$:$p \leq 0.05$, $^{\#\#}$: $p \leq 0.01$).

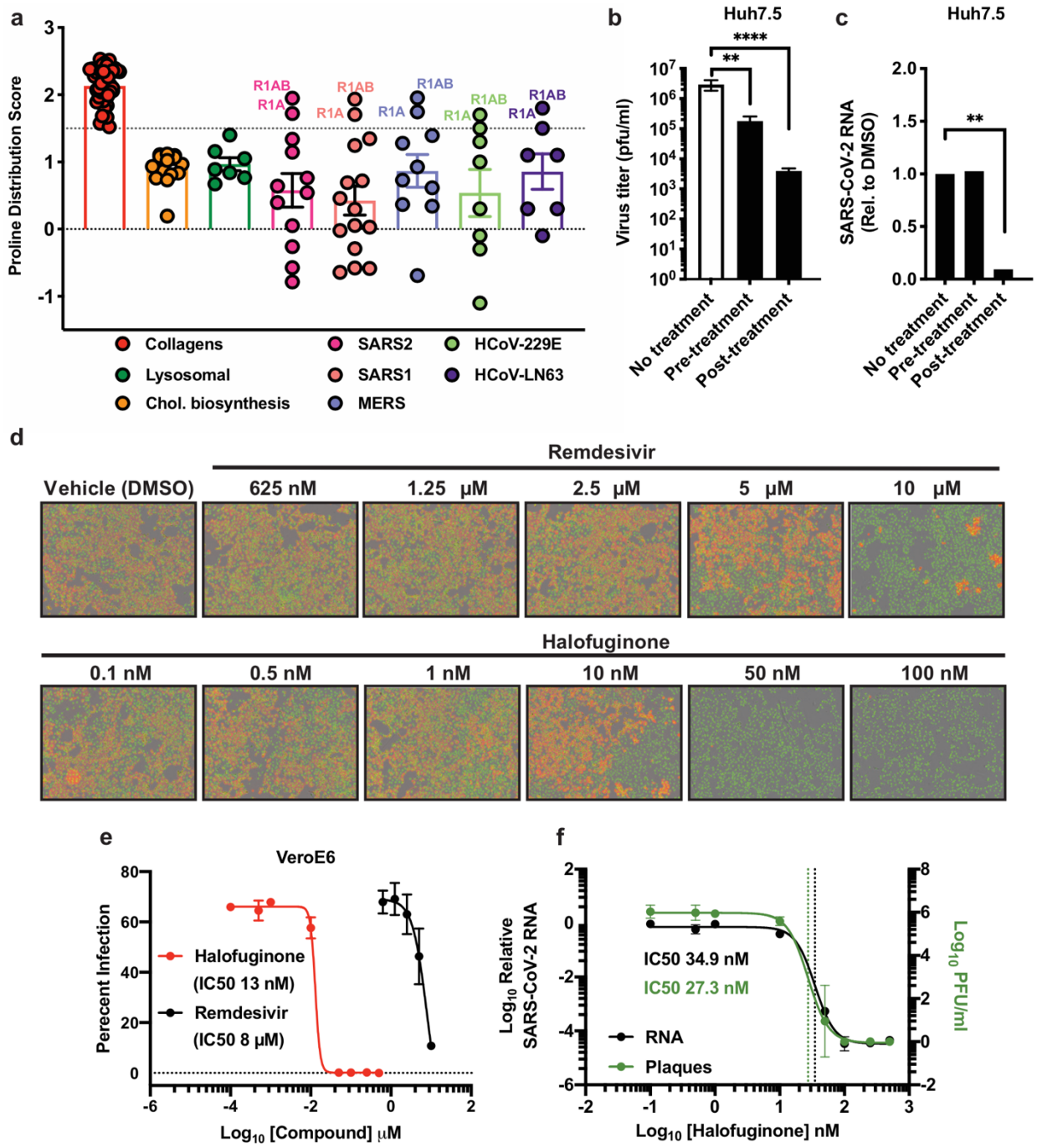

Figure 6. Halofuginone Inhibits infection and replication of authentic SARS-CoV-2. a, The proline distribution and density depicted as a proline distribution score for collagens, cholesterol biosynthetic proteins, lysosomal proteins and viral SARS-CoV-2 (SARS2), SARS-CoV-1 (SARS1), MERS-CoV (MERS), HCoV-229E and HCoV-LN63 proteins ($^{\#\#}p \leq 0.01$ collagens vs. all other protein classes). **b-c,** Authentic SARS-CoV-2 virus infection of Huh7.5 cells treated with

Halofuginone. Huh7.5 cells treated with halofuginone pre- or post-infection, or both pre- and post-infection with authentic SARS-CoV-2 virus. Viral titers (**b**) and quantification of viral RNA (**c**) in the infected cells is shown. **d,** Immunofluorescent quantification of viral nucleocapsid (red) protein in Vero E6 cells treated with halofuginone and remdesivir and infected with authentic SARS-CoV-2 virus (nuclei = green). **e,** Authentic SARS-CoV-2 virus infection of Vero E6 cells treated with halofuginone and remdesivir as measured in flow cytometry. **f,** Quantification of plaque formation and viral RNA in Vero E6 cells treated with halofuginone and remdesivir and infected with authentic SARS-CoV-2 virus. Data shown as mean ± S.D. Statistics performed by 1-way ANOVA and uncorrected Fisher's LSD test (ns: $p > 0.05$, **: $p \leq 0.01$, ***: $p \leq 0.001$, ****: $p \leq 0.0001$).

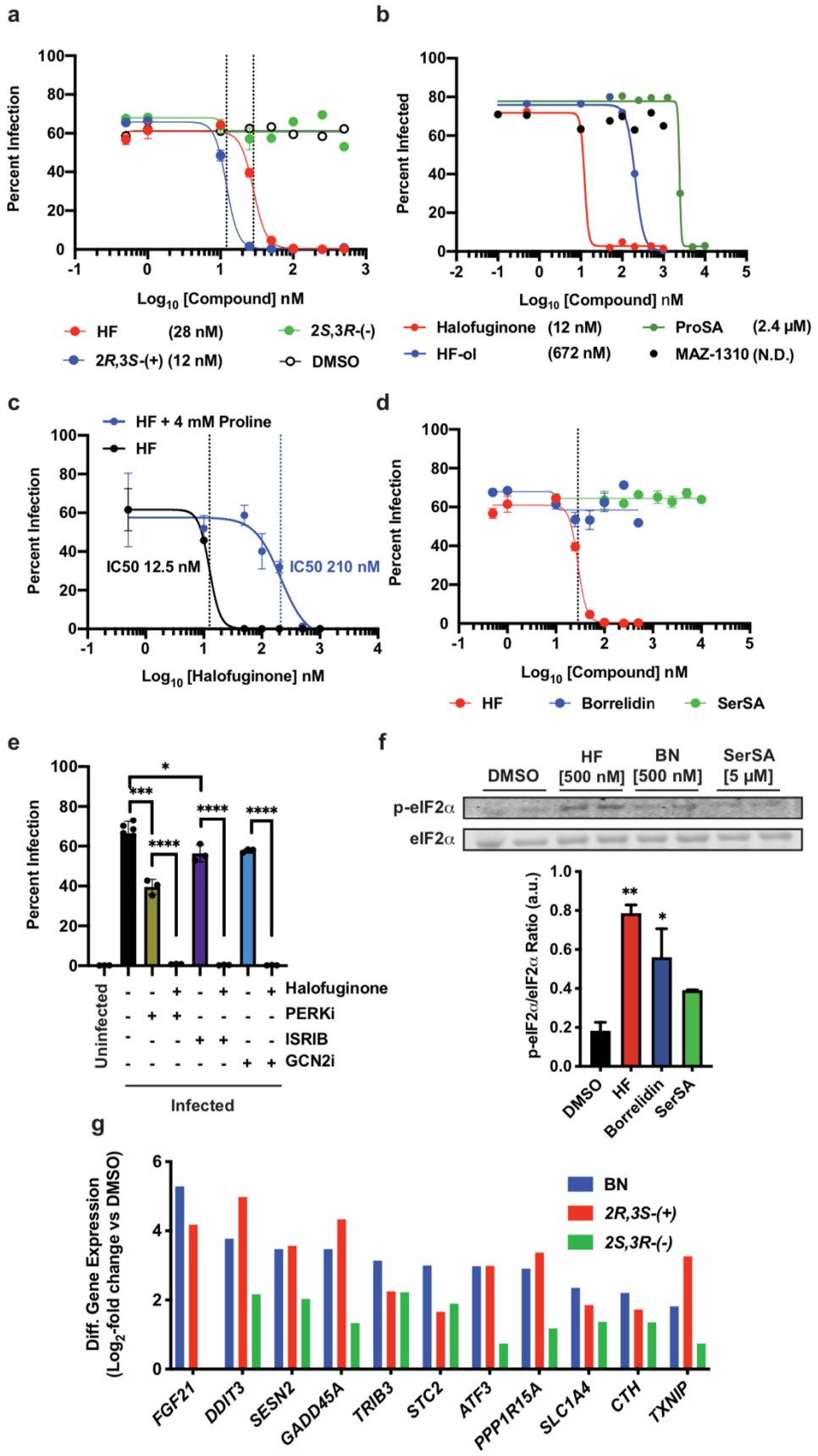
a
Percent Infection
Log10 [Compound] nM
HF (28 nM)
2R,3S-(+) (12 nM)
2S,3R-(-)
DMSO
b
Percent Infected
Log10 [Compound] nM
Halofuginone (12 nM)
HF-ol (672 nM)
ProSA (2.4 μM)
MAZ-1310 (N.D.)
c
HF + 4 mM Proline
HF
IC50 12.5 nM
IC50 210 nM
Percent Infection
Log10 [Halofuginone] nM
d
Percent Infection
Log10 [Compound] nM
HF
Borrelidin
SerSA
e
Percent Infection
Uninfected
Infected
Halofuginone
PERKi
ISRIB
GCN2i
f
DMSO
HF [500 nM]
BN [500 nM]
SerSA [5 μM]
p-eIF2α
eIF2α
p-eIF2α/eIF2α Ratio (a.u.)
DMSO
HF
Borrelidin
SerSA
g
Diff. Gene Expression (Log2-fold change vs DMSO)
BN
2R,3S-(+)
2S,3R-(-)
FGF21
DDIT3
SESN2
GADD45A
TRIB3
STC2
ATF3
PPP1R15A
SLC1A4
CTH
TXNIP

Figure 7. Halofuginone Inhibits infection and replication of authentic SARS-CoV-2 independent of the Integrated Stress Response. a, Post infection treatment of Vero E6 cells with halofuginone and enantiomers and their effect on authentic SARS-CoV-2 infection. **b,** Treatment of Vero E6 cells with modulators of the PRS pathway and their effect on SARS-CoV-2 infection. **c,** Rescue experiment of the effect of halofuginone treatment on SARS-CoV-2 infection using excess proline. **d,** Treatment of Vero E6 cells with AARS inhibitors, borrelidin and SerSA, and their effect on SARS-CoV-2 infection. **e,** Treatment of Vero E6 cells with modulators of the ISR pathway and their effect on SARS-CoV-2 infection. **f,** Immunoblot and quantification of total eIF2α versus phosphorylated eIF2α (p- eIF2α) in Vero E6 cells after a 2 hour incubation with halofuginone (HF), borrelidin (BN), or SerSA. **g**, RNA-Seq quantification of genes involved in the ATF4-mediated integrated stress response upon 6hr treatment of Vero E6 cell with borrelidin (BN) or halofuginone enantiomers when compared to DMOS treatment (average of n = 3 per group). Data shown as mean ± S.D. Statistics performed by 1-way ANOVA and uncorrected Fisher's LSD test (ns: $p > 0.05$, *: $p \leq 0.05$, **: $p \leq 0.01$, ***: $p \leq 0.001$, ****: $p \leq 0.0001$).

STAR METHODS

Reagents

SARS-CoV-2 (2019-nCoV) Spike Protein (RBD, His Tag) (Sino Biologicals, 40592-V08B), and proteins were biotinylated using EZ-Link™ Sulfo-NHS-Biotin, No-Weigh™ (Thermo Fisher Scientific, A39256). Heparin lyases were from IBEX pharmaceuticals, Heparinase I (IBEX, 60-012), Heparinase II (IBEX, 60-018), Heparinase III (IBEX, 60-020). Protein production reagents included, Pierce™ Protein Concentrators PES Thermo Scientific™, Pierce™ Protein Concentrator PES (Thermo Fisher Scientific, 88517) and Zeba™ Spin Desalting Columns, 40K MWCO, 0.5 mL (Thermo Fisher Scientific, 87766). ISR pathway inhibitors used are ISRIB (Sigma, SML0843), GSK2606414 (Sigma, 516535), and A-92 (Axon, 2720). Antibodies used were, anti-Spike antibody [1A9] (GeneTex, GTX632604), anti-Nucleocapsid antibody (GeneTex, GTX135357), Anti-HS (Clone F58-10E4) (Fisher Scientific, NC1183789), and 3G10 (BioLegend, 4355S). Secondary antibodies were, Anti-His-HRP (Genscript, A00612), Avidin-HRP (Biolegend, 339902), and Streptavadin-Cy5 (Thermo Fisher, SA1011). Luciferase activity was monitored by Bright-Glo™ (Promega, E2610). All cell culture medias and PBS where from Gibco.

Cell Culture

Huh-7.5 cells (Blight et al., 2002) were generously provided by Charles M. Rice (Rockefeller University, New York, NY). Hep3B, and BHK-15 were from ATCC and were grown in DMEM medium containing 10% % fetal bovine serum, and 100 IU/ml of penicillin, 100 µg/ml of streptomycin sulfate and nonessential amino acids. BHK-15 were grown in Modified Eagle's supplemented with 10% fetal bovine serum and nonessential amino acids (Gibco, #11140-050). Hep3B, A375 and Vero E6 cells were from ATCC. The Hep3B cells carrying mutations in HS biosynthetic enzymes was derived from the parent ATCC Hep3B stock, and have been described previously (Anower et al., 2020). All cells were supplemented with 10% FBS, 100 IU/ml of penicillin and 100 µg/ml of streptomycin sulfate and grown under an atmosphere of 5% CO2 and

95% air. Cells were passaged before 80% confluence was reached and seeded as explained for the individual assays. Cell viability was measured using LDH leakage (Promega) or alamarBleu (Thermo Fisher).

SARS-CoV-2 spike RBD protein production

Recombinant SARS-CoV-2 RBD (GenBank: MN975262.1; amino acid residues 319-529) was cloned into pVRC vector containing a HRV 3C-cleavable C-terminal SBP-His_{8X} tag was produced in ExpiCHO cells by transfection of 6 $x10^6$ cells/ml at 37 ºC with 0.8 μg/ml of plasmid DNA using the ExpiCHO expression system transfection kit in ExpiCHO Expression Medium (ThermoFisher). One day later the cells were fed with ExpiCho Feed, treated with ExpCho Enhancer, and then incubated at 32 ºC for 11 days. The conditioned medium was mixed with cOmplete EDTA-free Protease Inhibitor (Roche). Recombinant protein was purified by chromatography on a Ni^{2+} Sepharose 6 Fast Flow column (1 ml, GE LifeSciences). Samples were loaded in ExpiCHO Expression Medium supplemented with 30 mM imidazole, washed in a 20 mM Tris-Cl buffer (pH 7.4) containing 30 mM imidazole and 0.5 M NaCl. Recombinant protein was eluted with buffer containing 0.5 M NaCl and 0.3 M imidazole. The protein was further purified by size exclusion chromatography (HiLoad 16/60 Superdex 200, prep grade. GE LifeSciences) in 20 mM HEPES buffer (pH 7.4) containing 0.2 M NaCl.

SARS-CoV-2 Spike RBD Biotinylation

For binding studies, recombinant SARS-CoV-2 Spike RBD protein (RBD, His Tag) was conjugated with EZ-Link™ Sulfo-NHS-Biotin (1:3 molar ratio; Thermo Fisher) in Dulbecco's PBS at room temperature for 30 min. Glycine (0.1 M) was added to quench the reaction and the buffer was exchanged for PBS using a Zeba spin column (Thermo Fisher).

Flow cytometry

Cells at 50-70% confluence were treated with halofuginone or other inhibitors for 18-24 hrs. The cells were lifted with PBS containing 10 mM EDTA (Gibco) and washed in PBS containing 0.1% BSA. The cells were seeded into a 96-well plate at 10^5 cells per well. As a control for HS-dependent spike protein adhesion, a portion of the cells were treated with HSase mix (2.5 mU/ml HSase I, 2.5 or 5 mU/ml HSase II, and 5 mU/ml HSase III; IBEX) for 30 min at 37 ^oC in PBS containing 0.1% BSA. Cells were stained for 30 min at 4^oC with biotinylated spike RBD protein (20 µg/ml) or 10E4 mAB in PBS containing 0.1% BSA. The cells were washed twice and then reacted for 30 min at 4^oC with Streptavadin-Cy5 (Thermo Fisher; 1:1000 dilution) or anti-mouse IgG-Alexa488, respectively, in PBS containing 0.5% BSA. The cells were washed twice and then analyzed using a FACSCalibur or a FACSCanto instrument (BD Bioscience). All experiments were done a minimum of three separate times in three technical replicates. Data analysis was performed using FlowJo software and statistical analyses were done in Prism 8 (GraphPad).

HS and CS purification from cell surface of Hep3B cells

Fresh Hep3B cells were was washed in PBS, lifted with trypsin, and centrifuged for 5 min a 500 x g. The trypsin supernatants were saved for GAG analysis, and the cell pellets were washed in complete media, followed by a PBS wash, and saved for BCA analysis (Pierce™ BCA Protein Assay Kit, Themo Fisher), according to vendor specifications. The trypsin-released GAGs were treated with 1 mg/mL Pronase (Streptomyces griseus, Sigma Aldrich) and 0.1% Triton X-100 and 10 mM $CaCl_2$, and incubated at 37°C, overnight with shaking. The samples were centrifuged at 20,000 x g for 20 min and the supernatant was mixed 1:10 with equilibration buffer (50 mM sodium acetate, 0.2 M NaCl, 0.1% Triton X-100, pH 6) and loaded onto a DEAE Sephacel column (GE healthcare) equilibrated with equilibration buffer. The column was washed with wash buffer (50 mM sodium acetate, 0.2 M NaCl, pH 6.0) and bound GAGs were eluted with elution buffer (50 mM sodium acetate, 2.0 M NaCl, pH 6.0). The eluate was desalted using PD-10 columns (GE Healthcare) and lyophilized until dry.. The GAG pellets were reconstituted in DNase buffer (50

mM Tris, 50 mM NaCl, 2.5 mM $MgCl_2$, 0.5 mM $CaCl_2$, pH 8.0) with 20 kU/mL DNase I (Deoxyribonuclease I from Bovine Pancreas, Sigma Aldrich) and incubated for 2 hr at 37°C, shaking. Finally, the GAGs were purified over a DEAE column and precipitated by PD-10 chromatography (Esko, 1993).

HS and CS digestion and MS analysis

For HS quantification and disaccharide analysis, purified GAGs were digested with a mixture of heparin lyases I-III (2 mU each) for 2 hr at 37 °C in lyase buffer (40 mM ammonium acetate and 3.3 mM calcium acetate, pH 7.0). For CS quantification and disaccharide analysis, the GAGs were digested with 20 mU/mL Chondroitinase ABC (from Proteus vulgaris, Sigma Aldrich) and incubated for 2 hr at 37°C in lyase buffer (50 mM Tris and 50 mM NaCl, pH 8.0). The reactions were dried in a centrifugal evaporator and tagged by reductive amination with [$^{12}C_6$]aniline. The HS and CS samples were analyzed by liquid chromatography (LC) coupled to tandem mass spectrometry (MS/MS) and quantified by inclusion of [$^{13}C_6$]aniline-tagged standard HS disaccharides (Sigma-Aldrich), as described (Lawrence et al., 2008). The samples were separated on a reverse phase column (TARGA C18, 150 mm x 1.0 mm diameter, 5 µm beads, Higgins Analytical, Inc.) using 5 mM dibutylamine as an ion pairing agent (Sigma-Aldrich), and ions were monitored in negative mode. Separation was performed using the same gradient, capillary temperature, and spray voltage as described (Lawrence et al., 2008). The analysis was done on an LTQ Orbitrap Discovery electrospray ionization mass spectrometer (Thermo Scientific) equipped with an Ultimate 3000 quaternary HPLC pump (Dionex).

Western Blot Analysis

Cells were lysed using RIPA buffer, and protein was quantified using a BCA assay. Protein was analyzed by SDS-PAGE on 4–12% Bis-Tris gradient gels (NuPage; Invitrogen) with an equal amount of protein loading. Proteins were visualized after transfer to Immobilon-FL PVDF

membrane (Millipore). Membranes were blocked with Odyssey blocking buffer (LI-COR Biosciences) for 30 min and incubated overnight at 4°C with 3G10 antibodies. Mouse antibodies were incubated with secondary Odyssey IR dye antibodies (1:14,000) and visualized with an Odyssey IR imaging system (LI-COR Biosciences).

RNA-seq library preparation

Cells were lysed in Trizol and total RNA was extracted using the Direct-zol kit (Zymo Research, CA USA). On column DNA digestion was also performed with DNAse treatment. Poly(A) RNA was selected using the NEBNext Poly(A) mRNA Magnetic Isolation module (New England Biolabs) and libraries were prepared using the NEBNext Ultra Directional RNA Library Prep Kit (New England Biolabs) and sequenced using a NextSeq 500 (Illumina). Samples were sequenced at a minimum depth of 15 million reads per sample, paired end with a read length of 2x41bp.

RNA sequencing data analysis

A computational pipeline was written calling scripts from the CGAT toolkit to analyse the RNA sequencing data (https://github.com/cgat-developers/cgat-flow) (Cribbs AP, 2019; Sims et al., 2014). Briefly, FASTQ files were generated and assessed for quality using FASTQC, aligned to GRCh38 (hg38) and then aligned to the transcriptome using hisat2 v2.1.0 (Kim et al., 2019). To count mapped reads to individual genes, featurecounts v1.4.6, part of the subreads package (Liao et al., 2019), was used. Differential gene expression analysis was performed using DESeq2 using treatment and time as factors in the model. Genes were considered to be differentially expressed based on log2 fold change and p-value < 0.05. R scripts used to analyze the transcriptomic data are available through GitHub (https://github.com/Acribbs/deseq2_report). Motif enrichment was performed using homer as described before (Gordts et al., 2014; Heinz et al., 2010).

Preparation and infection by pseudotyped VSV

Vesicular Stomatitis Virus (VSV) pseudotyped with spike proteins of SARS-CoV-2 were generated according to a published protocol (Whitt, 2010). Briefly, HEK293T, transfected to express full length SARS-CoV-2 spike proteins, were inoculated with VSV-G pseudotyped ΔG-luciferase or GFP VSV (Kerafast, MA). After 2 hr at 37°C, the inoculum was removed and cells were refed with DMEM supplemented with 10% FBS, 50 U/mL penicillin, 50 µg/mL streptomycin, and VSV-G antibody (I1), mouse hybridoma supernatant from CRL-2700; ATCC). Pseudotyped particles were collected 20 hr post-inoculation, centrifuged at 1,320 × g to remove cell debris and stored at −80°C until use.

Cells were seeded at 10,000 cells per well in a 96-well plate. The cells were then treated with Halufuginone for 16hrs. As a control for HS dependent infection some cells were treated with HSases for 30 min at 37 ^{o}C in serum-free DMEM. Culture supernatant containing pseudovirus (20-100 µL) was adjusted to a total volume of 100 µL with PBS, HSase mix or the indicated inhibitors and the solution was added to the cells. After 4 hr at 37 ^{o}C the media was changed to complete DMEM. The cells were then incubated for 16 hr to allow expression of the luciferase gene. Cells were analyzed for infection by Bright-Glo^{TM} (Promega) using the manufacturers protocol. Briefly, 100 µL of luciferin lysis solution was added to the cells and incubated for 5 min at room temperature. The solution was transferred to a black 96-well plate and luminescence was detected using an EnSpire multimodal plate reader (Perkin Elmer). Data analysis and statistical analysis was performed in Prism 8.

SARS-CoV-2 infection

SARS-CoV-2 isolate USA-WA1/2020 (BEI Resources) was propagated and infectious units quantified by plaque assay using Vero E6 (ATCC) cells. Approximately 10e4 Vero E6 cells per well were seeded in a 96 well plate and incubated overnight. The following day, cells were washed with PBS and 100uL of SARS-CoV-2 (MOI 0.5) diluted in serum free DMEM was added per well and incubated 1 h at 37°C with rocking every 10-15 min. After 1 h, virus was removed, cells

washed with PBS and compounds or controls were added at the indicated concentrations. In experiments using inhibitors of the ISR or its related kinases, these compounds were added after viral infection and incubated for 1 h prior to the addition of HF. For viral RNA quantification, cells were washed twice with PBS and lysed in 200ul TRIzol (ThermoFisher). For immunofluorescence, cells were washed twice with PBS and incubated in 4% formaldehyde for 30 minutes at room temperature. For plaque assays, supernatant was removed and stored at -80 until plaque assays were performed.

Flavivirus and alphavirus infection

Sindbis virus (SINV) with mCherry-tagged NSP3 was propagated on BHK-15 cells (Jose et al., 2017). Uganda strain of Zika virus (ZIKV) MR 766 encoding the fluorescent protein Venus from the genome (a kind gift from Matthew Evans) was propagated on Huh 7.5 cells (Schwarz et al., 2016). Huh 7.5 and BHK-15 monolayers were pretreated with various halofuginone concentrations for 16 hours and infected with SINV or ZIKV at MOI of 0.1 for two hours in the presence of the compound. Subsequently, media over cells were replaced with fresh media containing halofuginone and incubated for 12 hours for SINV and 24 hours for ZIKV. The cell culture supernatants were collected at 12 hours post infection for SINV and 24 hours post infection for ZIKV and the virus titers were determined by fluorescent focus assay (FFT).

Methods for human bronchial epithelial cell ALI generation and infection

Air Liquid Interface

Human Bronchial Epithelial Cells (HBECs, Lonza) were cultured in T75 flasks in PneumaCult-Ex Plus Medium according to manufacturer instructions (StemCell Technologies). To generate air-liquid interface cultures, HBECs were plated on collagen I-coated 24 well transwell inserts with a 0.4-micron pore size (Costar, Corning) at $5x10^4$ cells/ml. Cells were maintained for 3-4 days in PneumaCult-Ex Plus Medium until confluence, then changed to PneumaCult-ALI Medium

(StemCell Technologies) containing ROCK inhibitor (Y-27632, Tocris) for 4 days. Fresh medium, 100 µl in the apical chamber and 500 µl in the basal chamber, was added daily. At day 7, the medium in the apical chambers was removed, and the basal chambers were changed every 2-3 days with apical washes with PBS every week for 28 days.

Human bronchial epithelial cell ALI Infection.

The apical side of the HBEC ALI culture was gently washed three times with 200 µl of phosphate buffered saline without divalent cations (PBS-/-). An MOI of 0.5 of SARS-CoV-2 live virus in 100 µl total volume of PBS was added to the apical chamber with either DMSO, Heparinase or or various halofuginone concentrations. Cells were incubated at *37◦C* and 5% CO2 for 4 hours. Unbound virus was removed, the apical surface was washed and the compounds were re-added to the apical chamber. Cells were incubated for another 20 hours at *37◦C* and 5% CO2. After inoculation, cells were washed once with PBS-/- and 100 µl TrypLE (ThermoFisher) was added to the apical chamber then incubated for 10 min in the incubator. Cells were gently pipetted up and down and transferred into a sterile 15 ml conical tube containing neutralizing medium of DMEM + 3% FBS. TrypLE was added again for 3 rounds of 10 minutes for a total of 30 min to clear transwell membrane. Cells were spun down and resuspended in PBS with Zombie UV viability dye for 15 min in room temp. Cells were washed once with FACS buffer then fixed in 4% PFA for 30 min at room temp. PFA was washed off and cells were resuspended in PBS.

Virus plaque assays

Confluent monolayers of Vero E6 or Hep3B cells were infected with SARS-CoV-2 at an MOI of 0.1. After one hour of incubation at 37 °C, the virus was removed, and the medium was replaced. After 48 hr, cell culture supernatants were collected and stored at -80°C. Virus titers were determined by plaque assays on Vero E6 monolayers. In short, serial dilutions of virus stocks in Dulbecco's Modified Essential Media (DMEM) (Corning, #10-014-CV) were added to Vero E6 monolayers on 12-well plates and incubated 1 hr at 37 °C with rocking every 10-15 min. The cells

were subsequently overlaid with MEM containing 0.6% agarose (ThermoFisher Scientific, #16500-100), 4% FBS, non-essential amino acids, L glutamine, and sodium bicarbonate and the plates were incubated at 37 °C under an atmosphere of 5% CO_2/95% air for 48 hr. The plates were fixed with a mixture of 10% formaldehyde and 2% methanol (v/v in PBS) for 24 hr. Agarose overlays were removed, and the monolayer was washed once with PBS and stained with 0.025% Crystal Violet prepared in 2% ethanol. After 15 min, Crystal Violet was removed, and plaques were counted to determine the virus titers. Plaque assays were performed and counted by a blinded experimenter. All work with SARS-CoV-2 was conducted in Biosafety Level-3 conditions either at the University of California San Diego or at the Eva J Pell Laboratory, The Pennsylvania State University, following the guidelines approved by the Institutional Biosafety Committees.

RNA extraction, cDNA synthesis and qPCR:

RNA was purified from TRIzol lysates using Direct-zol RNA Microprep kits (Zymo Research) according to manufacturer recommendations that included DNase treatment. RNA was converted to cDNA using the iScript cDNA synthesis kit (BioRad) and qPCR was performed using iTaq universal SYBR green supermix (BioRad) and an ABI 7300 real-time pcr system. cDNA was amplified using the following primers RPLP0 F – GTGTTCGACAATGGCAGCAT; RPLP0 R – GACACCCTCCAGGAAGCGA; SARS-CoV-2 Spike F – CCTACTAAATTAAATGATCTCTGCTTTACT; SARS-CoV-2 Spike R – CAAGCTATAACGCAGCCTGTA. Relative expression of SARS-CoV-2 Spike RNA was calculated by delta-delta-Ct by first normalizing to the housekeeping gene RPLP0 and then comparing to SARS-CoV-2 infected Vero E6 cells that were untreated (reference control). Curves were fit and inhibitory concentration (IC) IC50 and IC90 values calculated using Prism 8.

Immunofluorescence imaging and analysis

Formaldehyde fixed cells were washed with PBS and permeabilized for immunofluorescence using BD Cytofix/Cytoperm according to the manufacturers protocol for fixed cells and stained for SARS-CoV-2 with a primary anti-Nucleocapsid antibody (GeneTex GTX135357) followed by a secondary Goat anti Rabbit AF594 antibody (ThermoFisher A-11037) and nuclei stained with Sytox Green. Five or eight images per well were obtained using an Incucyte S3 (Sartorius) or Nikon Ti2-E microscope equipped with a Qi-2 camera and Lumencor Spectra III light engine respectively. The percent infected cells were calculated using built-in image analysis tools for the Incucyte S3. For images acquired with the Nikon Ti2, images were analysed using the Fiji distribution of ImageJ (PMID 22743772) and the DeepLearning plugin StarDist as follows. Channels were separated and the Sytox Green-stained nuclei were segmented using StarDist to generate individual masks for each nucleus. The AF594 channel (Nucleocapsid) was selected by removing background with a rolling ball of 50 pixels. A median filter (sigma=10) was applied to facilitate easier thresholding of AF594 signal. The resulting image was thresholded and a mask was generated representing all positive staining. Positive nuclei were selected by firstly eroding the StarDist generated nuclei mask by 2 pixels to reduce potential overlap with non-positive stain. Binary reconstruction was then carried out between the resulting mask and the AF594 mask. Uwe Schmidt, Martin Weigert, Coleman Broaddus, and Gene Myers. Cell Detection with Star-convex Polygons. International Conference on Medical Image Computing and Computer-Assisted Intervention (MICCAI), Granada, Spain, September 2018.

Proline distribution analysis

Protein amino acid sequences were downloaded from UniProtKB (UniProt, 2019). Proline distribution was analyzed using custom code in R (v3.6.0) (Team, 2019), including commands from the packages dplyr (H. Wickham, 2020) tidyr (Wickham, 2020), and stringr (Wickham, 2019). All plots were generated in ggplot2 (Wickham, 2016). For individual protein plots, histograms were constructed with geom_histogram(binwidth = 1) and kernel density estimations (KDEs) were

constructed with geom_density(kernel = “gaussian”) and added as custom annotations (ggpubr package (Kassambara, 2020)). The bandwidth of KDEs for individual plots was assessed separately for each protein distribution using maximum likelihood cross-validation (Duin, 1976; J.D.F. Habbema, 1974) with the h.mlcv command from the kedd package (Guidoum, 2015). The proline distribution score was calculated using the following formula:

$$Proline\ dist.score = \log_{10}({}^{B_P}/_{B_T} * P)$$

where B_P is the number of 10-amino acid blocks in a protein that contain one or more prolines (a protein with length 100 amino acids has 10 blocks); B_T is the total number of 10-amino acid blocks in a protein; and P is the total number of prolines in a protein. B_P values were obtained using custom code in R.

Data and Code availability

Data are deposited in the National Centre for Biotechnology Information GEO database under the accession number (GSE157036). Depicted structures have been solved and deposited: halofuginone PDB ID 4K88, ProSA PDB ID 5V58, and NCP22 PDB ID 5VAD. The custom-scripted macro used for automated image analysis of live cell imaging data is available from https://doi.org/10.26180/5f508284eb365. Code and files used for proline analysis can be found on https://github.com/jkccoker/Proline_analysis.

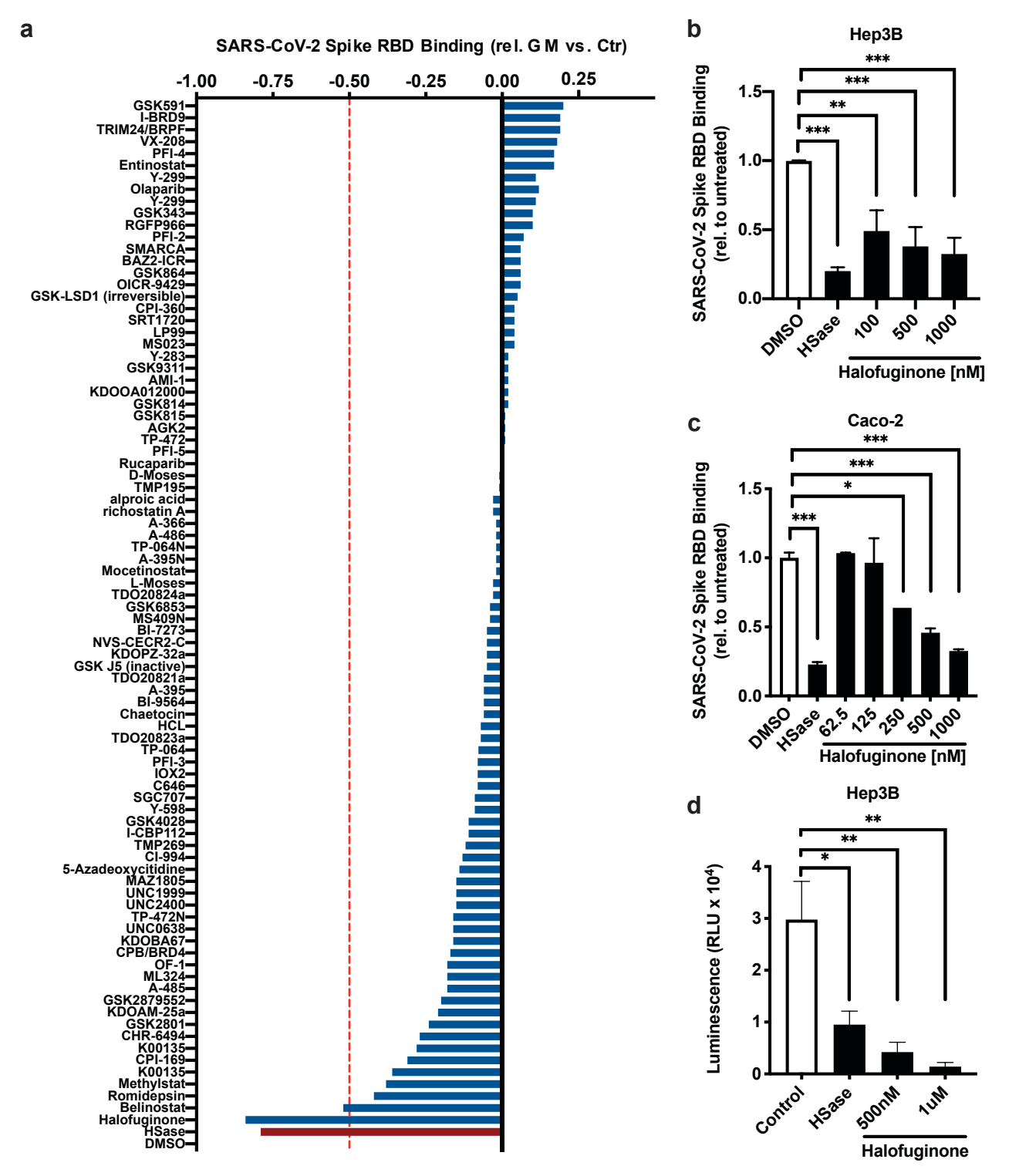
a
SARS-CoV-2 Spike RBD Binding (rel. GM vs. Ctr)
-1.00
-0.75
-0.50
-0.25
0.00
0.25
GSK591
I-BRD9
TRIM24/BRPF
VX-208
PFI-4
Entinostat
Y-299
Olaparib
Y-299
GSK343
RGFP966
PFI-2
SMARCA
BAZ2-ICR
GSK864
OICR-9429
GSK-LSD1 (irreversible)
CPI-360
SRT1720
LP99
MS023
Y-283
GSK9311
AMI-1
KDOOA012000
GSK814
GSK815
AGK2
TP-472
PFI-5
Rucaparib
D-Moses
TMP195
alproic acid
richostatin A
A-366
A-486
TP-064N
A-395N
Mocetinostat
L-Moses
TDO20824a
GSK6853
MS409N
BI-7273
NVS-CECR2-C
KDOPZ-32a
GSK J5 (inactive)
TDO20821a
A-395
BI-9564
Chaetocin
HCL
TDO20823a
TP-064
PFI-3
IOX2
C646
SGC707
Y-598
GSK4028
I-CBP112
TMP269
CI-994
5-Azadeoxycitidine
MAZ1805
UNC1999
UNC2400
TP-472N
UNC0638
KDOBA67
CPB/BRD4
OF-1
ML324
A-485
GSK2879552
KDOAM-25a
GSK2801
CHR-6494
K00135
CPI-169
K00135
Methylstat
Romidepsin
Belinostat
Halofuginone
HSase
DMSO
b
Hep3B
SARS-CoV-2 Spike RBD Binding (rel. to untreated)
1.5
1.0
0.5
0.0
***
***
**
***
DMSO
HSase
100
500
1000
Halofuginone [nM]
c
Caco-2
SARS-CoV-2 Spike RBD Binding (rel. to untreated)
1.5
1.0
0.5
0.0
***
***
*
***
DMSO
HSase
62.5
125
250
500
1000
Halofuginone [nM]
d
Hep3B
Luminescence (RLU x 10⁴)
4
3
2
1
0
**
**
*
Control
HSase
500nM
1uM
Halofuginone

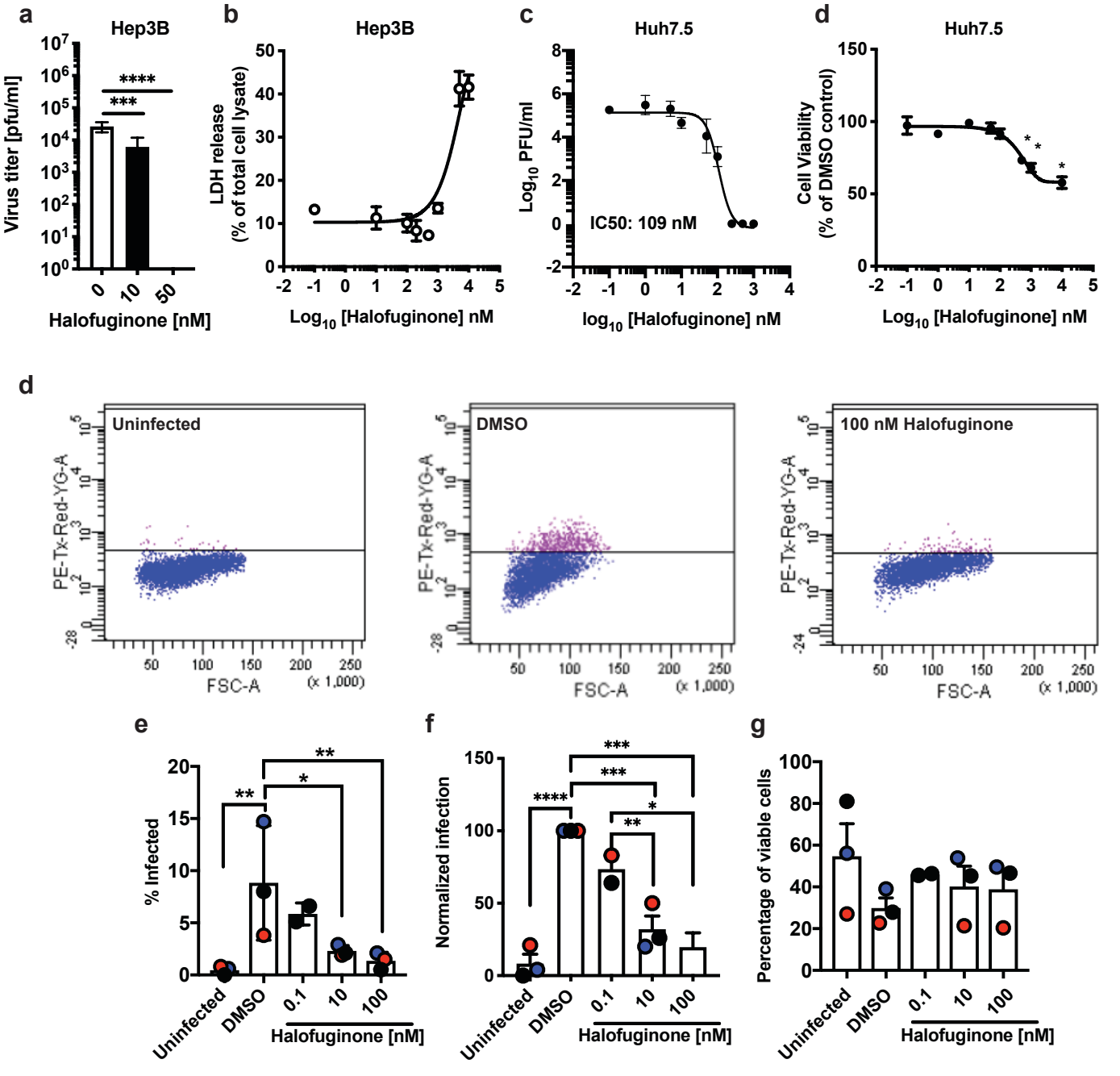
a
Hep3B
Virus titer [pfu/ml]
****
***
Halofuginone [nM]
b
Hep3B
LDH release
(% of total cell lysate)
Log10 [Halofuginone] nM
c
Huh7.5
Log10 PFU/ml
IC50: 109 nM
log10 [Halofuginone] nM
d
Huh7.5
Cell Viability
(% of DMSO control)
Log10 [Halofuginone] nM
d
Uninfected
DMSO
100 nM Halofuginone
PE-Tx-Red-YG-A
FSC-A
(x 1,000)
e
% Infected
Uninfected
DMSO
Halofuginone [nM]
f
Normalized infection
Uninfected
DMSO
Halofuginone [nM]
g
Percentage of viable cells
Uninfected
DMSO
Halofuginone [nM]

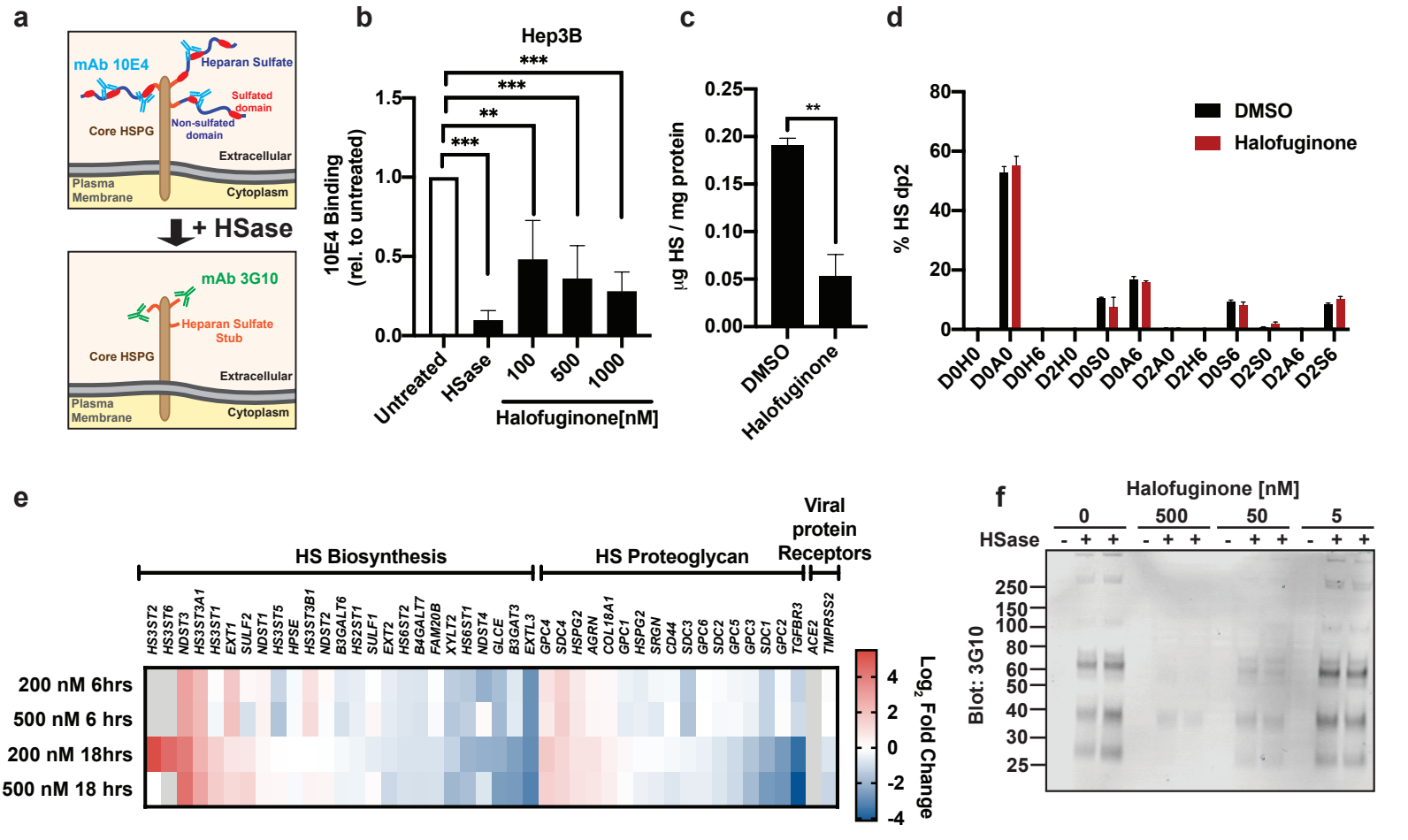
a
mAb 10E4
Heparan Sulfate
Sulfated domain
Core HSPG
Non-sulfated domain
Extracellular
Plasma Membrane
Cytoplasm
+ HSase
mAb 3G10
Heparan Sulfate Stub
Core HSPG
Extracellular
Plasma Membrane
Cytoplasm
b
Hep3B
10E4 Binding (rel. to untreated)
Untreated
HSase
100
500
1000
Halofuginone[nM]
c
µg HS / mg protein
DMSO
Halofuginone
d
% HS dp2
DMSO
Halofuginone
D0H0
D0A0
D0H6
D2H0
D0S0
D0A6
D2A0
D2H6
D0S6
D2S0
D2A6
D2S6
e
HS Biosynthesis
HS Proteoglycan
Viral protein Receptors
HS3ST2
HS3ST6
NDST3
HS3ST3A1
HS3ST1
EXT1
SULF2
NDST1
HS3ST5
HPSE
HS3ST3B1
NDST2
B3GALT6
HS2ST1
SULF1
EXT2
HS6ST2
B4GALT7
FAM20B
XYLT2
HS6ST1
NDST4
GLCE
B3GAT3
EXTL3
GPC4
SDC4
HSPG2
AGRN
COL18A1
GPC1
HSPG2
SRGN
CD44
SDC3
GPC6
SDC2
GPC5
GPC3
SDC1
GPC2
TGFBR3
ACE2
TMPRSS2
200 nM 6hrs
500 nM 6 hrs
200 nM 18hrs
500 nM 18 hrs
Log2 Fold Change
f
Halofuginone [nM]
0
500
50
5
HSase
Blot: 3G10

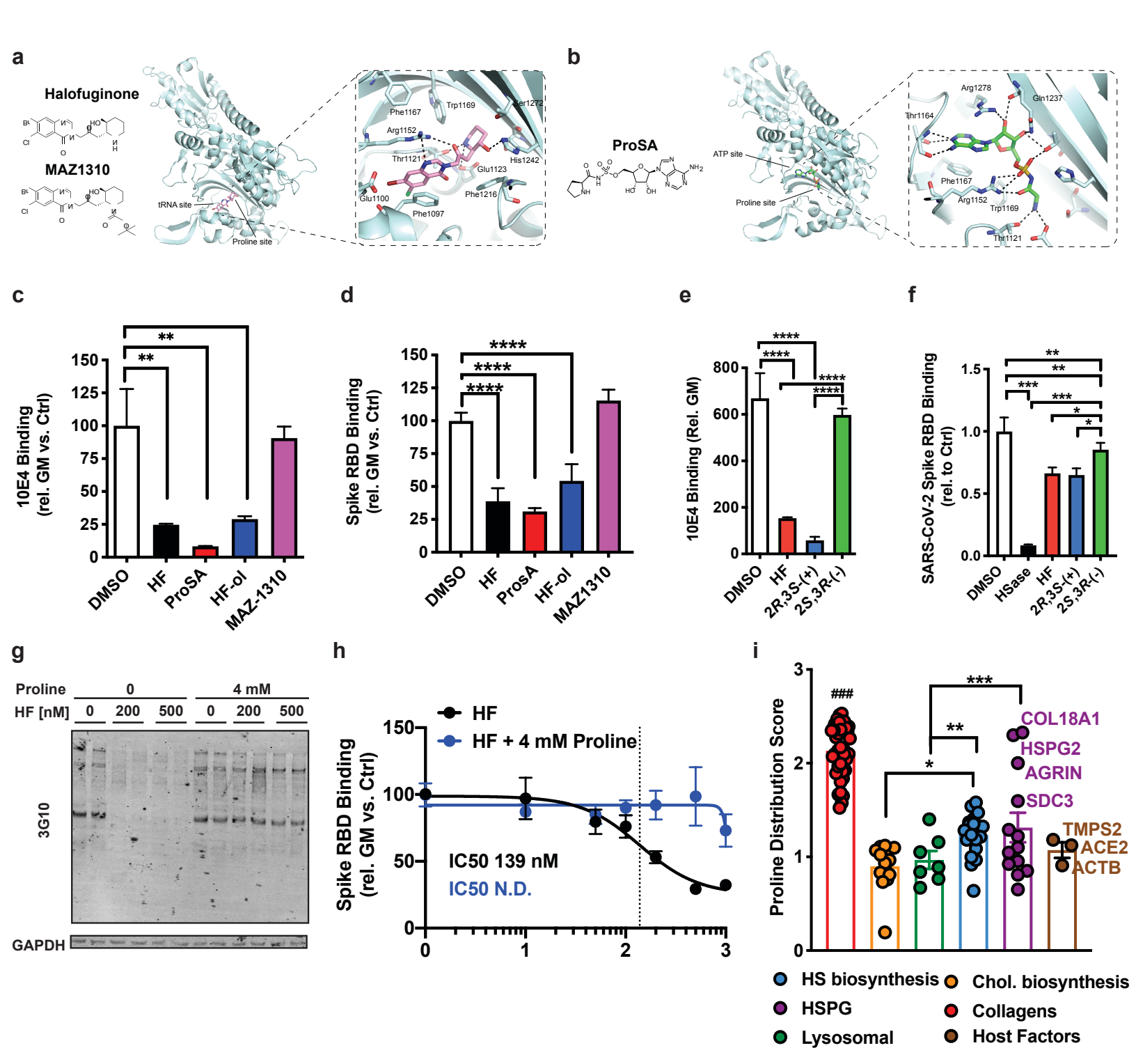
a
Halofuginone
MAZ1310
tRNA site
Proline site
Phe1167
Trp1169
Ser1272
Arg1152
Thr1121
His1242
Glu1123
Glu1100
Phe1216
Phe1097
b
ProSA
ATP site
Proline site
Arg1278
Gln1237
Thr1164
Phe1167
Arg1152
Trp1169
Thr1121
c
10E4 Binding (rel. GM vs. Ctrl)
DMSO
HF
ProSA
HF-ol
MAZ-1310
d
Spike RBD Binding (rel. GM vs. Ctrl)
DMSO
HF
ProsA
HF-ol
MAZ1310
e
10E4 Binding (Rel. GM)
DMSO
HF
2R,3S-(+)
2S,3R-(-)
f
SARS-CoV-2 Spike RBD Binding (rel. to Ctrl)
DMSO
HSase
HF
2R,3S-(+)
2S,3R-(-)
g
Proline
0
4 mM
HF [nM]
0
200
500
0
200
500
3G10
GAPDH
h
HF
HF + 4 mM Proline
Spike RBD Binding (rel. GM vs. Ctrl)
IC50 139 nM
IC50 N.D.
i
Proline Distribution Score
COL18A1
HSPG2
AGRIN
SDC3
TMPS2
ACE2
ACTB
HS biosynthesis
Chol. biosynthesis
HSPG
Collagens
Lysosomal
Host Factors

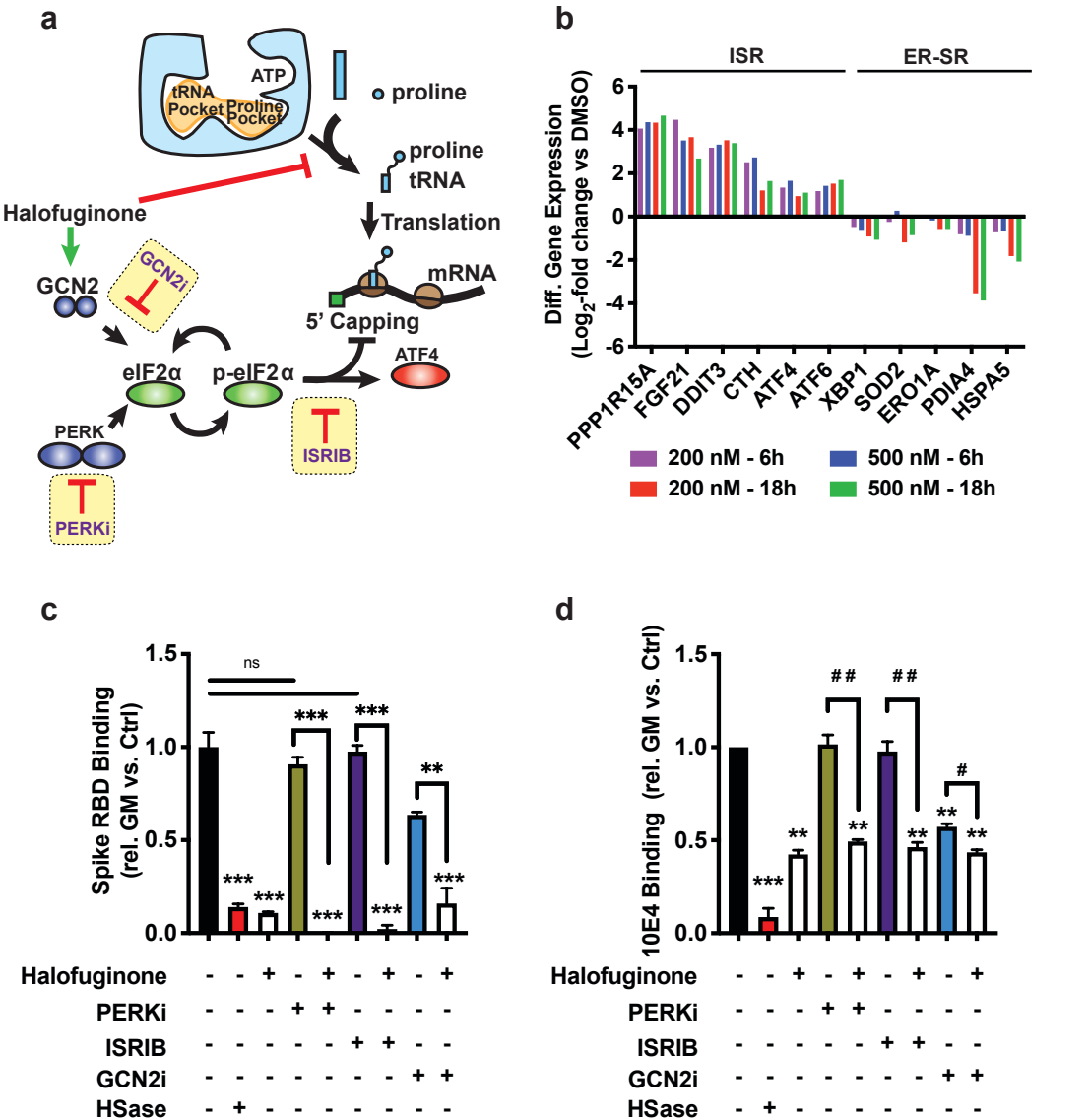
a
ATP
tRNA Pocket
Proline Pocket
proline
proline tRNA
Translation
mRNA
5' Capping
ATF4
Halofuginone
GCN2
GCN2i
eIF2α
p-eIF2α
PERK
PERKi
ISRIB
b
ISR
ER-SR
Diff. Gene Expression (Log2-fold change vs DMSO)
PPP1R15A
FGF21
DDIT3
CTH
ATF4
ATF6
XBP1
SOD2
ERO1A
PDIA4
HSPA5
200 nM - 6h
200 nM - 18h
500 nM - 6h
500 nM - 18h
c
Spike RBD Binding (rel. GM vs. Ctrl)
ns
Halofuginone
PERKi
ISRIB
GCN2i
HSase
d
10E4 Binding (rel. GM vs. Ctrl)
Halofuginone
PERKi
ISRIB
GCN2i
HSase

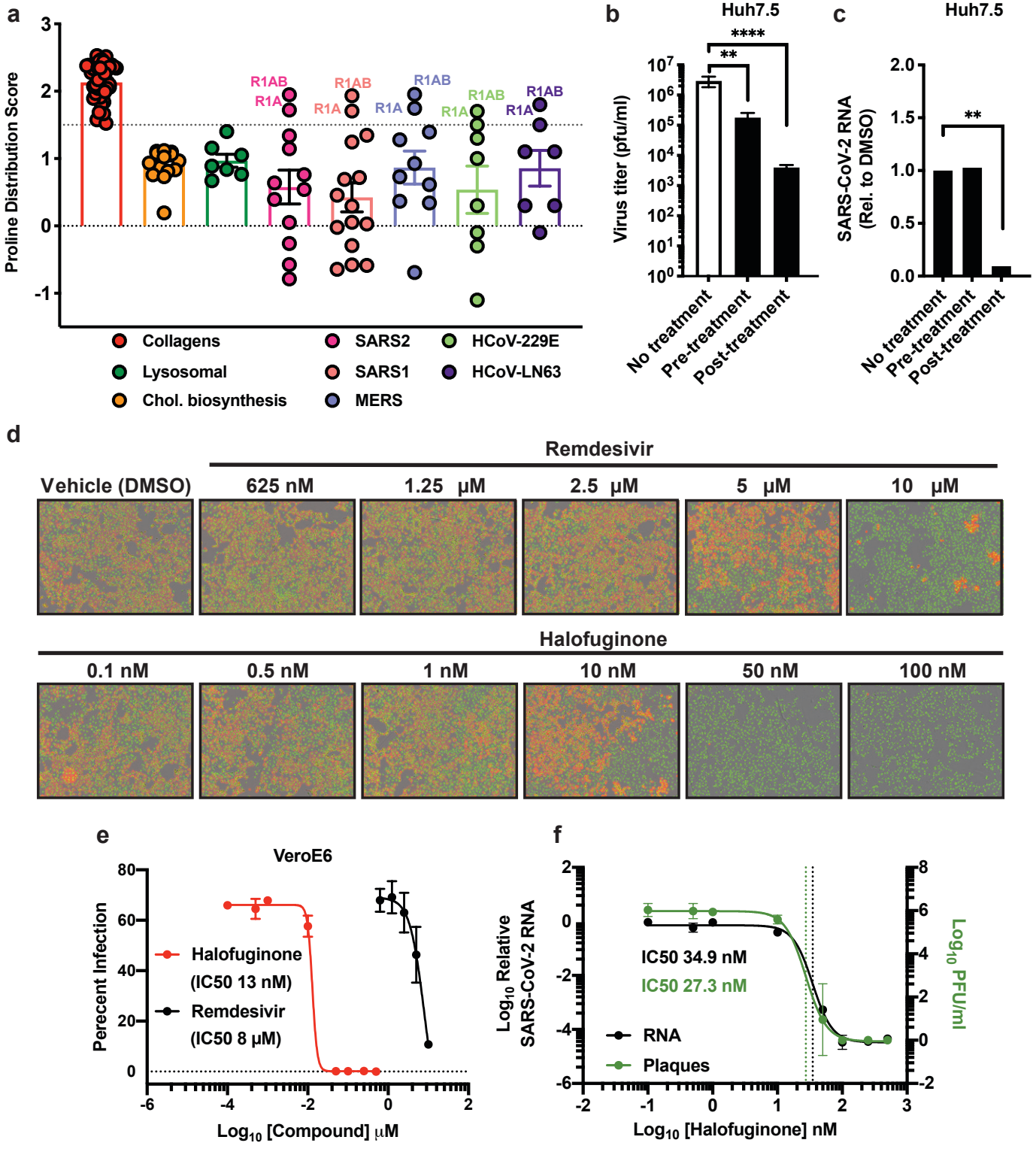
a
Proline Distribution Score
R1AB
R1A
Collagens
Lysosomal
Chol. biosynthesis
SARS2
SARS1
MERS
HCoV-229E
HCoV-LN63
b
Huh7.5
Virus titer (pfu/ml)
No treatment
Pre-treatment
Post-treatment
c
Huh7.5
SARS-CoV-2 RNA (Rel. to DMSO)
d
Remdesivir
Vehicle (DMSO)
625 nM
1.25 μM
2.5 μM
5 μM
10 μM
Halofuginone
0.1 nM
0.5 nM
1 nM
10 nM
50 nM
100 nM
e
VeroE6
Perecent Infection
Halofuginone (IC50 13 nM)
Remdesivir (IC50 8 μM)
Log10 [Compound] μM
f
Log10 Relative SARS-CoV-2 RNA
Log10 PFU/ml
IC50 34.9 nM
IC50 27.3 nM
RNA
Plaques
Log10 [Halofuginone] nM

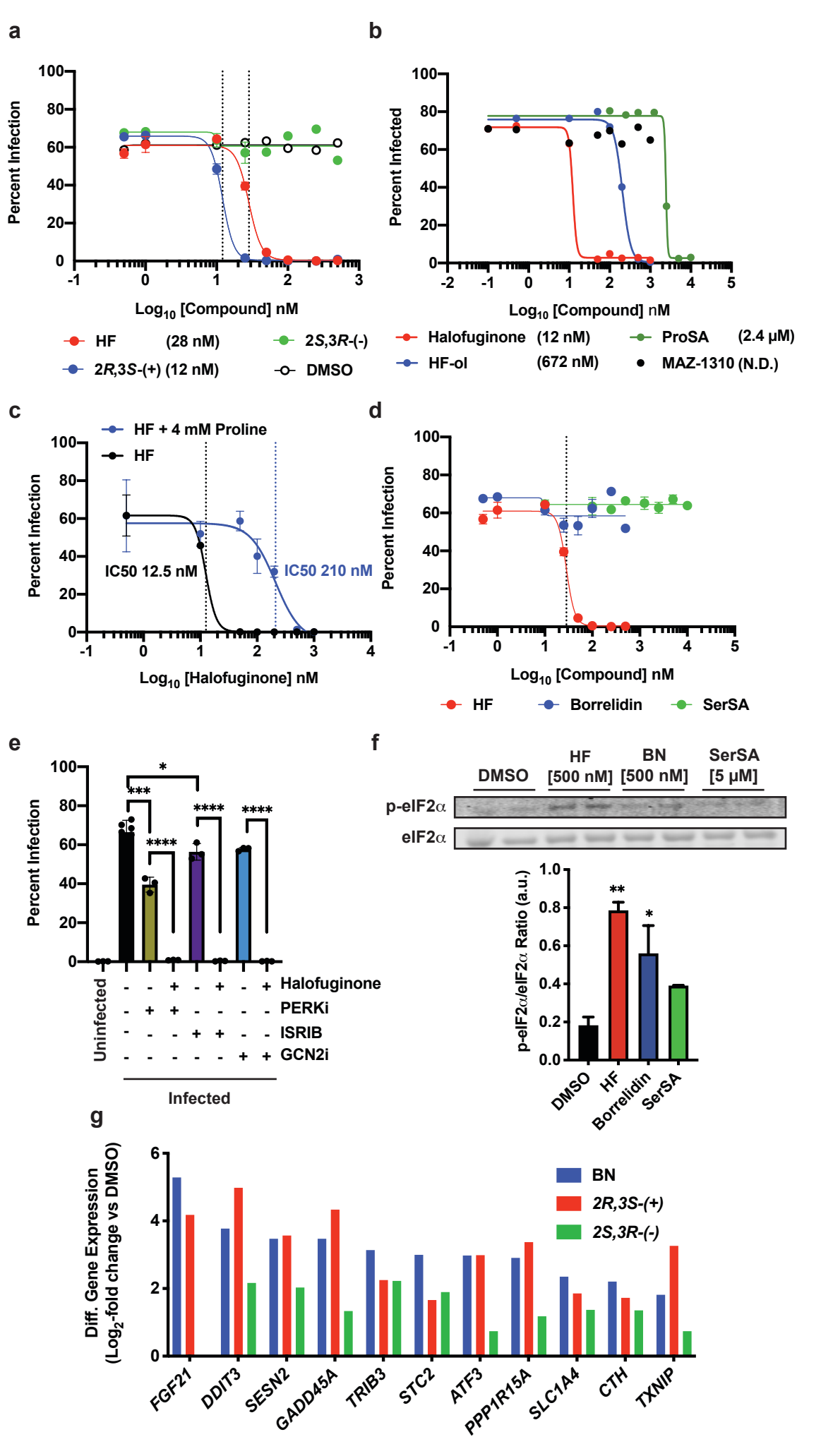
a
Percent Infection
Log10 [Compound] nM
HF (28 nM)
2R,3S-(+) (12 nM)
2S,3R-(-)
DMSO
b
Percent Infected
Log10 [Compound] nM
Halofuginone (12 nM)
HF-ol (672 nM)
ProSA (2.4 μM)
MAZ-1310 (N.D.)
c
HF + 4 mM Proline
HF
IC50 12.5 nM
IC50 210 nM
Percent Infection
Log10 [Halofuginone] nM
d
Percent Infection
Log10 [Compound] nM
HF
Borrelidin
SerSA
e
Percent Infection
Uninfected
Infected
Halofuginone
PERKi
ISRIB
GCN2i
f
DMSO
HF [500 nM]
BN [500 nM]
SerSA [5 μM]
p-eIF2α
eIF2α
p-eIF2α/eIF2α Ratio (a.u.)
DMSO
HF
Borrelidin
SerSA
g
Diff. Gene Expression (Log2-fold change vs DMSO)
BN
2R,3S-(+)
2S,3R-(-)
FGF21
DDIT3
SESN2
GADD45A
TRIB3
STC2
ATF3
PPP1R15A
SLC1A4
CTH
TXNIP